Icarus 209 (2010) 195–209

Contents lists available at ScienceDirect

Icarus

journal homepage: www.elsevier.com/locate/icarus

Identification and measurement of neutron-absorbing elements on Mercury's surface

David J. Lawrence [a,*], William C. Feldman [b], John O. Goldsten [a], Timothy J. McCoy [c], David T. Blewett [a], William V. Boynton [d], Larry G. Evans [e], Larry R. Nittler [f], Edgar A. Rhodes [a], Sean C. Solomon [f]

[a] Johns Hopkins University Applied Physics Laboratory, Laurel, MD 20723, USA
[b] Planetary Science Institute, 1700 East Fort Lowell, Suite 106, Tucson, AZ 85719, USA
[c] National Museum of Natural History, Smithsonian Institution, Washington, DC 20560, USA
[d] University of Arizona, Lunar and Planetary laboratory, 1629 E. University Blvd., Tucson, AZ 85721, USA
[e] Computer Sciences Corporation, Lanham-Seabrook, MD 20706, USA
[f] Carnegie Institution of Washington, Washington, DC 20015, USA

ARTICLE INFO

Article history:
Received 23 October 2009
Revised 24 March 2010
Accepted 8 April 2010
Available online 13 April 2010

Keyword:
Mercury, surface

ABSTRACT

MESSENGER Neutron Spectrometer (NS) observations of cosmic-ray-generated thermal neutrons provide the first direct measurements of Mercury's surface elemental composition. Specifically, we show that Mercury's surface is enriched in neutron-absorbing elements and has a measured macroscopic neutron-absorption cross section of 45–81 $\times 10^{-4}$ cm^2/g, a range similar to the neutron absorption of lunar basalts from Mare Crisium. The expected neutron-absorbing elements are Fe and Ti, with possible trace amounts of Gd and Sm. Fe and Ti, in particular, are important for understanding Mercury's formation and how its surface may have changed over time through magmatic processes. With neutron Doppler filtering – a neutron energy separation technique based on spacecraft velocity – we demonstrate that Mercury's surface composition cannot be matched by prior models, which have characteristically low abundances of Fe, Ti, Gd, and Sm. While neutron spectroscopy alone cannot separate the relative contributions of individual neutron-absorbing elements, these results provide strong new constraints on the nature of Mercury's surface materials. For example, if all the measured neutron absorption were due to the presence of an Fe–Ti oxide and that oxide were ilmenite, then Mercury's surface would have an ilmenite content of 7–18 wt.%. This result is in general agreement with the inference from color imaging and visible-near-infrared spectroscopy that Mercury's overall low reflectance is consistent with a surface composition that is enriched in Fe–Ti oxides. The incorporation of substantial Fe and Ti in oxides would imply that the oxygen fugacity of basalts on Mercury is at the upper range of oxygen fugacities inferred for basalts on the Moon.

1. Introduction

Despite many measurements from Earth and from the Mariner 10 spacecraft, there is little definitive information about the elemental composition of Mercury's surface (Goettel, 1988; Taylor and Scott, 2003). Specifically, there has been much debate about the Fe content of Mercury's surface materials (e.g., Sprague et al., 2007; Boynton et al., 2007). For example, 1-μm absorption bands resulting from Fe^{2+} in silicates are either absent or very weak in reflectance spectra of Mercury at visible to near-infrared wavelengths. Taken at face value, these observations have been interpreted to imply that the FeO concentration of both the crust and the mantle of Mercury must be very low. This conclusion contrasts with the fact that the high uncompressed density of Mercury indicates that some 60% of its mass must be iron metal. The surface Fe content may be an important discriminator for testing whether Mercury's high bulk metal fraction stemmed from aerodynamic drag in the early solar nebula (Weidenschilling, 1978), from preferential vaporization of silicates by an early hot solar nebula (Cameron, 1985; Fegley and Cameron, 1987), or from loss of the planet's original silicate crust and much of its mantle during a giant impact (Wetherill, 1988; Benz et al., 1988). Although we have only limited information on the abundance of FeO in Mercury's crust, information on the abundances of other key elements (e.g., Ca, Si, Mg, K, Ti) that are concentrated in planetary crusts during differentiation is even more restricted. Ti may be particularly informative, since, like FeO, it appears to be low in abundance in Mercury surface silicates (Warell and Blewett, 2004), but it couples with iron in a variety of Fe–Ti-oxides in crustal rocks on other bodies.

* Corresponding author. Address: Johns Hopkins University Applied Physics Laboratory, MP3-E169, 11100 Johns Hopkins Drive, Laurel, MD 20723, USA.
E-mail address: David.J.Lawrence@jhuapl.edu (D.J. Lawrence).

0019-1035/$ - see front matter © 2010 Elsevier Inc. All rights reserved.
doi:10.1016/j.icarus.2010.04.005

In 2008 and 2009, the MErcury Surface, Space ENvironment, GEochemistry, and Ranging (MESSENGER) spacecraft performed three flybys of Mercury (Solomon et al., 2008; Denevi et al., 2009) en route to insertion into orbit about the innermost planet in March 2011. Data from MESSENGER's Mercury Atmospheric and Surface Composition Spectrometer (MASCS) (McClintock et al., 2008) confirmed the absence of the 1-μm absorption feature expected for Fe^{2+} in silicates, in agreement with the earlier ground-based studies. Recent analyses of Mariner 10 (Denevi and Robinson, 2008) and MESSENGER Mercury Dual Imaging System (MDIS) color images (Denevi et al., 2009) and ground-based mid-infrared emission observations (Sprague et al., 2007, 2009) have led to the suggestion that Mercury's surface may have substantially more Fe and Ti in the form of oxides (e.g., ilmenite, $FeTiO_3$, or rutile, TiO_2) than was previously suspected. We note that all of these inferences are from spectral observations sensitive to mineralogical variations rather than elemental abundances. Moreover, spectral observations are affected by factors (e.g., space weathering, grain size variations) that are at best only partially understood but can cause variations unrelated to composition (e.g., Noble and Pieters, 2003).

We present in this paper the first analysis of neutron measurements from Mercury directly sensitive to the abundances of neutron-absorbing elements on Mercury's surface. We utilize observations by MESSENGER's Neutron Spectrometer (NS), which is part of the Gamma-Ray and Neutron Spectrometer (GRNS) instrument (Goldsten et al., 2007). Neutrons are produced on airless or nearly airless planetary bodies when galactic cosmic rays (GCRs) hit the surface, which occurs when any atmosphere is too thin to absorb the GCRs and the magnetic field is too low in magnitude to deflect them. Neutrons are produced by GCR-induced spallation reactions with energies in the range 1–100 MeV, down-scatter in energy through many orders of magnitude, and finally reach energies that are in thermal equilibrium with the planetary surface. A portion of these neutrons at all energies escapes to space and can be detected by a neutron sensor near the planet. The flux of thermal neutrons is highly sensitive to the presence of neutron-absorbing elements at the planet's surface. For solid planets with little to no hydrogen, the dominant neutron-absorbing elements are Fe and Ti. At sufficiently high abundances (tens of parts per million), Gd and Sm also cause measurable absorption of thermal neutrons because of their extremely large thermal neutron-absorption cross sections. The utility of thermal neutrons for measuring Fe, Ti, Gd, and Sm abundances has been demonstrated with the Lunar Prospector mission at the Moon (Feldman et al., 1998, 2000; Elphic et al., 1998, 2000, 2002). Although thermal neutrons cannot discriminate among different absorbing elements, they provide a highly sensitive measure of the presence and total abundance of all neutron-absorbing elements. Further, thermal neutrons provide depth-integrated measurements from up to a meter below the surface. Because neutron spectroscopy is not sensitive to the various mineralogical, space weathering, or grain-size effects inherent to spectral reflectance techniques, it provides a direct, complementary, and independent assessment of Mercury's surface elemental composition.

2. Neutron Spectrometer on the MESSENGER spacecraft

The MESSENGER NS (Fig. 1) consists of three scintillators that are each separately read out with photomultiplier tubes (PMTs) (Goldsten et al., 2007). The center block, a borated plastic (BP) scintillator, is sensitive to epithermal (0.4 eV to 500 keV) and fast neutrons (500 keV to few MeV), and the two planar lithium glass (LG) scintillators are sensitive to thermal (<0.4 eV) and epithermal neutrons. The NS is attached to the MESSENGER spacecraft on the side opposite the sunshade and is located close to one of three co-aligned spacecraft fuel tanks (Leary et al., 2007). The NS is positioned on the spacecraft so that the normal to the LG1 sensor points in the direction of the spacecraft $+x$-axis and the normal to the LG2 sensor points in the direction of the spacecraft $-x$-axis. These and other axes in the local spacecraft coordinate system are shown in Fig. 1.

The NS is designed to separately measure thermal and epithermal neutrons using the Doppler filter technique (Feldman and Drake, 1986). This technique takes advantage of the similarity in velocity between the spacecraft and thermal neutrons. An enhancement of thermal neutrons is measured when the spacecraft velocity vector is in line with the sensor normal vector; a relative decrease in thermal neutrons is measured when the spacecraft velocity vector is anti-parallel to the sensor normal. Finally, no Doppler effect occurs when the spacecraft velocity vector is perpendicular to the sensor normal vector.

3. Neutron Spectrometer data from three Mercury flybys

The MESSENGER spacecraft completed three flybys of Mercury on January 14, 2008 (M1), October 6, 2008 (M2), and September 29, 2009 (M3). Neutron data were collected during all three flybys, but different altitude-dependent spacecraft rotation maneuvers enabled measurements more sensitive to surface composition to be collected during M1 and M3 than during M2.

Pulse-height spectra from each LG sensor for M1 are shown in Fig. 2. Although not shown here, pulse-height data from M2 and M3 are similar. The peaks around channel 25 in each sensor are due to 4.78-MeV energy deposition from the $^6Li(n,\alpha)^3H$ reaction when neutrons are absorbed by the LG sensors. The averaged background is subtracted from the data near closest approach (CA) to give a net peak from the neutron detections (solid blue trace in Fig. 2). Except for excess counts at low-energy channels that are likely due to planetary gamma-rays, the net counts are well fit by a Gaussian function (dashed blue curve) that is similar in width to pre-launch calibration data (Goldsten et al., 2007). To avoid including any counts from the gamma-ray background in the summed neutron counts, we define the total measured neutron counts in each sensor as the total counts above channel 17. To account for neutrons not included in the low-channel Gaussian tail (i.e., since we are measuring counts above channel 17), we multiply the total counts by normalization factors that are dependent on the specific detector gain and energy resolution. More details of this data reduction process are given in Appendix A.

During each flyby, NS data were collected in 2-s time increments. These 2-s data were combined into 60-s time bins and the resulting time-series counting rates for M1, M2, and M3 are shown in Figs. 3–5. The error bars for the LG1 and LG2 counting rates are the 1-σ uncertainties from Poisson counting statistics, where σ is the estimated standard deviation (Bevington and Robinson, 1992) determined from the individual uncertainties of both the flyby and background data (see Appendix A). Figs. 3–5 also show spacecraft altitude and orientation information. The spacecraft orientation parameter most relevant to the NS is $\mathbf{V}\cdot\hat{x}/|\mathbf{V}|$, where $\mathbf{V}$ is the spacecraft vector velocity, and $\hat{x}$ is the spacecraft x-axis unit vector. $\mathbf{V}\cdot\hat{x}/|\mathbf{V}|$ gives a measure of the Doppler-filter effect: $\mathbf{V}\cdot\hat{x}/|\mathbf{V}| = +1$ indicates a thermal neutron enhancement for the LG1 sensor and $\mathbf{V}\cdot\hat{x}/|\mathbf{V}| = -1$ indicates a thermal neutron enhancement for the LG2 sensor. Figs. 3–5 show that as the spacecraft altitude decreases, the neutron counting rate in both LG sensors generally increases with peak counting rates near CA. The detailed time profile is substantially different between the two sensors. For M1 and M2, the LG1 profile generally shows a monotonic rise to CA with a slower fall after CA. For M3, the data stop at 21:48 UTC due to the fact that the MESSENGER spacecraft went

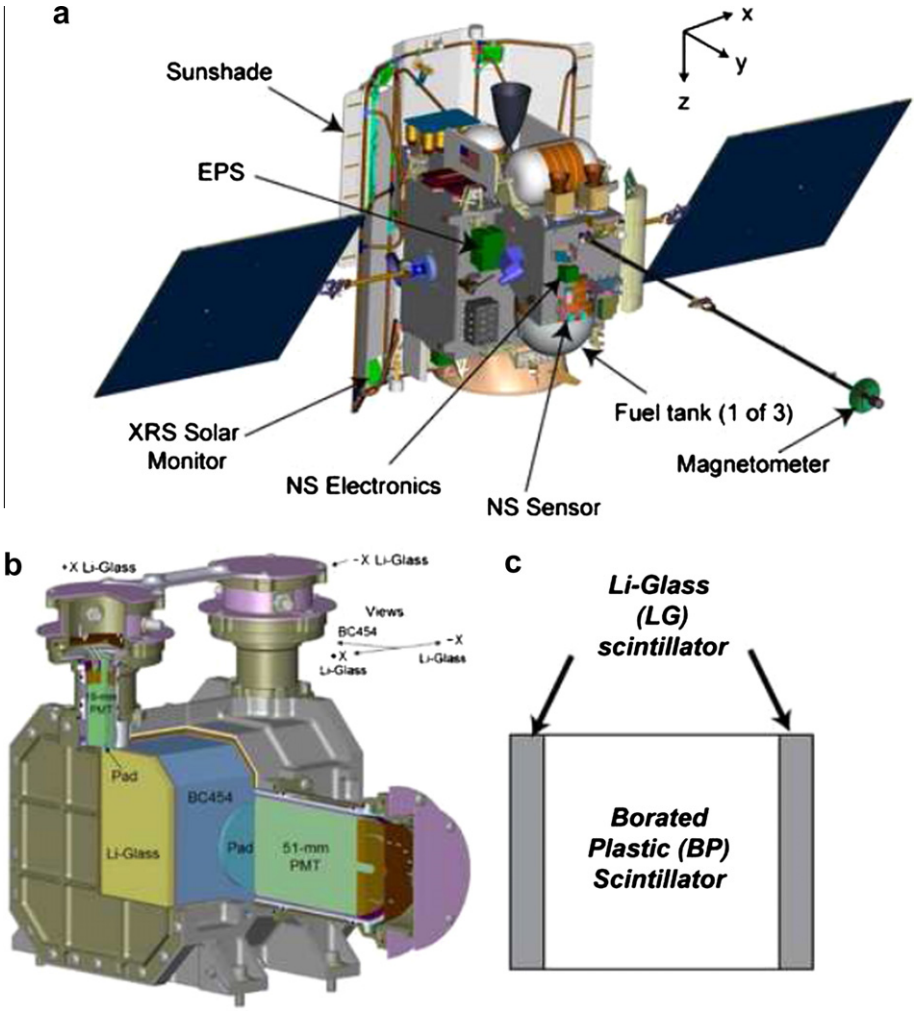

Fig. 1. (a) Locations of the Neutron Spectrometer (NS sensor) and NS electronics on the MESSENGER spacecraft (Leary et al., 2007) relative to the sunshade at the left and the three fuel tanks that shield the NS from the Sun. (b) A drawing of the MESSENGER NS, and (c) a simplified schematic of the placement of the three NS sensor components. The term BC454 in (b) refers to the designation of the borated plastic scintillator in (c).

into safe mode and shut down all science data collection. In contrast to the LG1 data, LG2 data show a variety of local maxima prior to CA. For M1, two local maxima coincide in time with local minima in $\mathbf{V}\cdot\hat{x}/|\mathbf{V}|$ at 18:50 and 18:59 UTC, indicating that these peaks are, in part, the result of Doppler-enhanced thermal neutrons. Doppler-filter peaks from LG2 are also seen for M2 and M3 at 8:32 UTC and 21:48 UTC, respectively. Another partial cause of the time-dependent behavior of the LG2 time profile is time-dependent spacecraft obscuration and attenuation of neutrons from Mercury as the spacecraft rotated during the flyby. Fig. 6 shows the Mercury ground tracks during M1, M2, and M3, the sub-spacecraft points at CA and the thermal neutron enhancements, and full-width, half-maximum (FWHM) spatial footprints, which are based on the spacecraft altitude (Lawrence et al., 2003; Maurice et al., 2004).

The MESSENGER NS also measures fast neutrons, which can be used to determine the average atomic mass of a non-hydrous planetary soil (Maurice et al., 2000; Gasnault et al., 2001). Information about Mercury's average atomic mass, however, has not been derived from MESSENGER flyby data for two reasons. First, the fast neutron response of the NS has not yet been modeled. Second, the limited flyby data are likely insufficient to provide the relative variations over Mercury's surface needed to understand clearly the composition dependence of the fast neutron flux.

4. Modeling of Neutron Spectrometer data

To understand the relative effects of Doppler thermal neutron enhancement and spacecraft obscuration and attenuation, and more generally how the NS data are related to Mercury's surface composition, the neutron transport from Mercury's surface to the NS must be modeled. Specifically, the neutron transport properties of the spacecraft materials need to be explicitly taken into account. Feldman et al. (1989) gave a generalized expression for the neutron counting rate, C, measured from a spacecraft moving around a planet:

$$C = \frac{N}{2\pi}\int d\varphi \int d\mu \int dK \frac{\mathbf{V}_T\cdot\hat{n}}{|\mathbf{V}|} A\varepsilon(\varphi_D,\mu_D,K_D)\Phi(\varphi,\mu,K). \quad (1)$$

The integral is calculated over angular variables φ and $\mu=\cos(\theta)$ from within a spacecraft nadir-fixed coordinate system (where φ is the azimuth angle and θ is the polar angle relative to the nadir direction) and energy K. The GCR-induced neutron flux at orbital altitude, Φ (assumed to be azimuthally symmetric), is modeled for a variety of surface compositions and is calculated in terms of neutrons per incident GCR proton per cm^2. An overall normalization factor, N, includes factors to account for the absolute GCR flux. The area-efficiency response of the NS, which includes

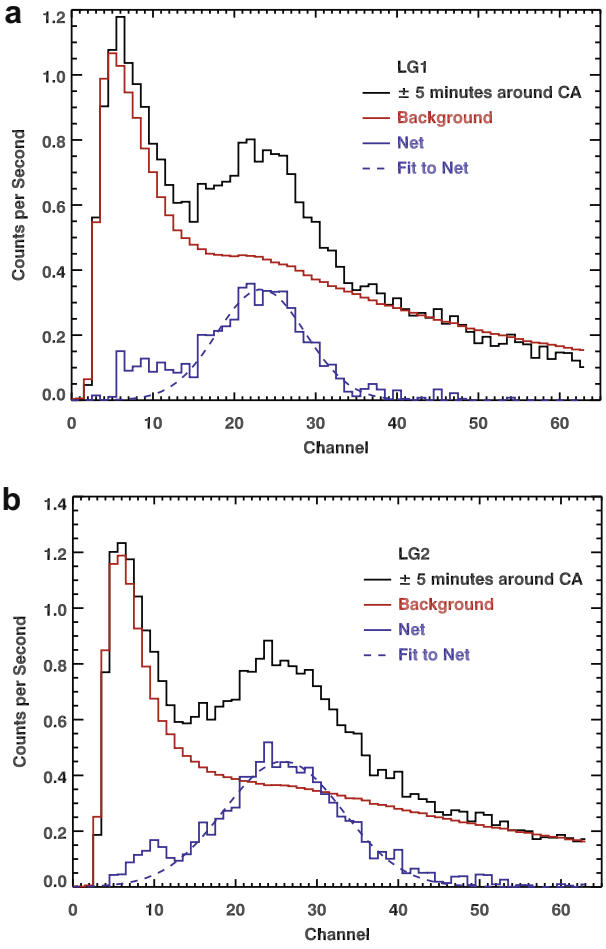

Fig. 2. MESSENGER NS pulse-height data from M1 for (a) the LG1 and (b) LG2 sensors. In each plot, data taken within 5 min of closest approach are shown by the black line. Averaged data taken for one day both before and after closest approach are shown by the red line. Net data (black line minus the red line) are shown by the blue line. A Gaussian fit to the net data is shown by the dashed blue line.

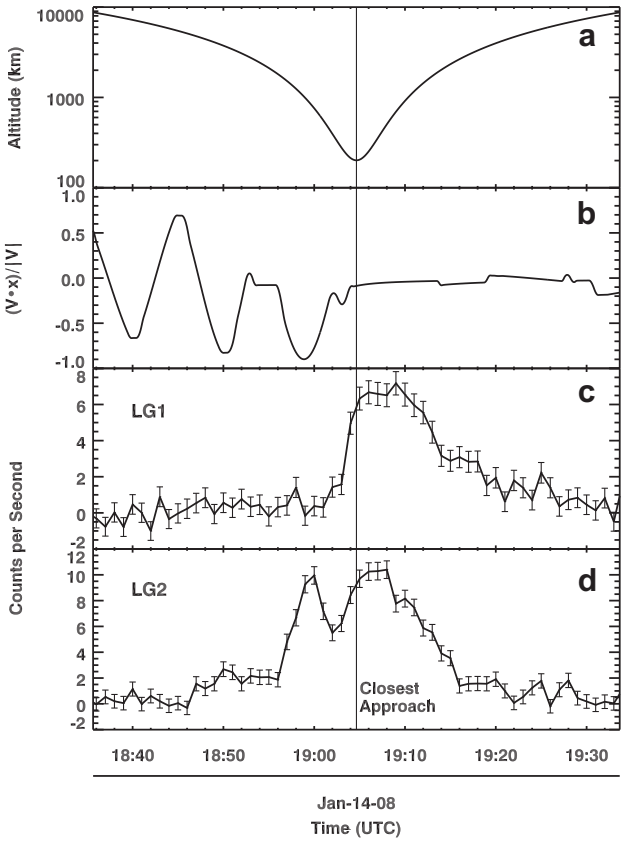

Fig. 3. MESSENGER NS data from M1. (a) Spacecraft altitude versus time. (b) $\mathbf{V}\cdot\hat{x}/|\mathbf{V}|$ versus time. (c) LG1 data in 60-s increments versus time. (d) LG2 data in 60-s increments versus time. The vertical line at 19:05 UTC denotes closest approach.

the neutron response of the spacecraft, is given by $A\varepsilon$, where A is the detector area and ε is the detector efficiency. ε is dependent on spacecraft-fixed angles and energies (φ_D, μ_D, K_D), which themselves are dependent on the spacecraft nadir-fixed angles and energies. Eq. (1) includes a velocity dot-product term, where $\hat{n}$ is the unit vector normal to the sensor being modeled, $\mathbf{V}_T$ is the velocity of the neutron in the frame of the detector, and $\mathbf{V}$ is the velocity of the neutron at the altitude of detection. A summary of how the two main terms in Eq. (1) are calculated – surface neutron flux and NS area-efficiency response – is given below.

4.1. Calculation of Mercury's surface neutron flux

The surface neutron flux from Mercury was calculated in a manner similar to previous calculations for lunar soils (McKinney et al., 2006; Lawrence et al., 2006). We used the Monte Carlo particle transport code MCNPX (Pelowitz, 2005) and provided an initial GCR proton flux to model the neutron production, transport, and absorption from a spherical Mercury surface. The effects of gravity and finite neutron lifetime were explicitly taken into account. For a GCR energy-dependent flux spectrum, we used the parameterization for protons and alpha particles given by Masarik and Reedy (1996) that depends on a solar modulation parameter, ϕ, which affects both the shape and absolute normalization of the spectrum. To obtain the solar modulation parameter, we used the procedure of McKinney et al. (2006) and Earth-based south-pole neutron monitor data (Bartol Research Institute, 2009) to estimate that $\phi = 300$ MV during the time of M1. The total GCR normalization for $\phi = 300$ MV and protons greater than 30 MeV is $N_{GCR} = 6.4$ equivalent protons cm^{-2} s^{-1}, where the contribution from alpha particles was calculated according to the procedure given by McKinney et al. (2006).

We calculated neutron fluxes for a variety of temperatures from 70 to 700 K that span the range of expected Mercury surface temperatures. Because all the flyby data were taken on the Mercury night side, we used a temperature of 100 K for the results reported here. For model Mercury surface compositions, we used seven returned lunar soil compositions that span a wide range of neutron absorption from a soil low in Fe, Ti, Gd, and Sm (ferroan anorthosite, FAN) to a soil high in Fe, Ti, Gd, and Sm (Apollo 11). Further, all these soils have a low hydrogen content that is appropriate for non-polar surfaces on the Moon and Mercury. Table 1 lists these soils, their elemental compositions, the elemental microscopic neutron-absorption cross section, σ_a, for each element in the soil, and the total macroscopic neutron-absorption cross section, Σ_a, for each soil. Σ_a parameterizes the neutron absorbing ability of a soil and is defined by a weighted sum over elements i: $\Sigma_a = \sum_i \sigma_{a,i} f_i N_A / A_i$, where f_i is the elemental weight fraction, A_i is the atomic mass of element i, and N_A is Avogadro's number. To more finely tune the modeled Σ_a values, we also considered two variants of the Luna 24 soil composition, for which we lowered the Fe contents of the Luna 24 soil from 15 wt.% to 12.5 wt.% and 10 wt.% and the remaining mass was assigned to Mg. For this purpose, Mg is an appropriate Fe substitute because Mg has a low σ_a, and Mg can typically substitute for Fe in a variety of minerals.

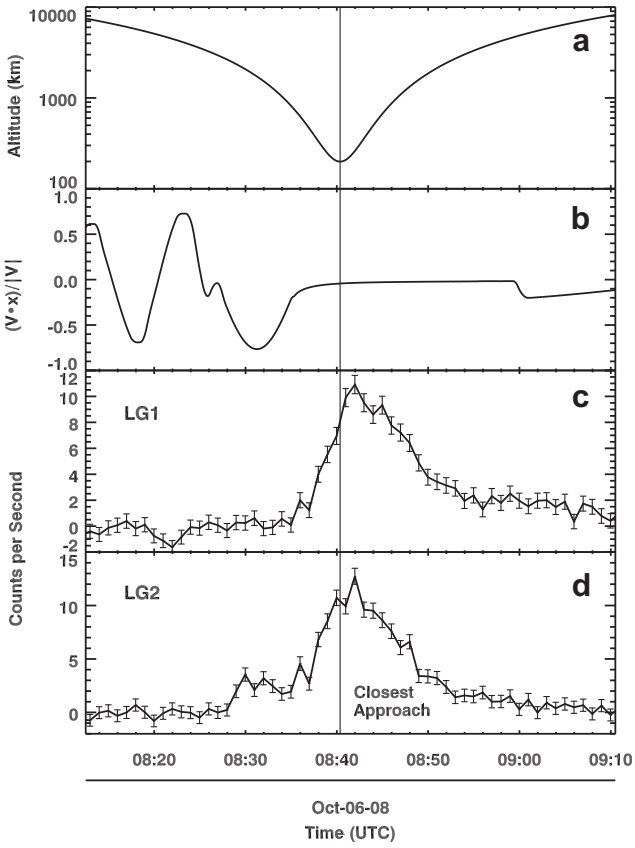

Fig. 4. MESSENGER NS data from M2. (a) Spacecraft altitude versus time. (b) $\mathbf{V}\cdot\hat{x}/|\mathbf{V}|$ versus time. (c) LG1 data in 60-s increments versus time. (d) LG2 data in 60-s increments versus time. The vertical line at 8:40 UTC denotes closest approach.

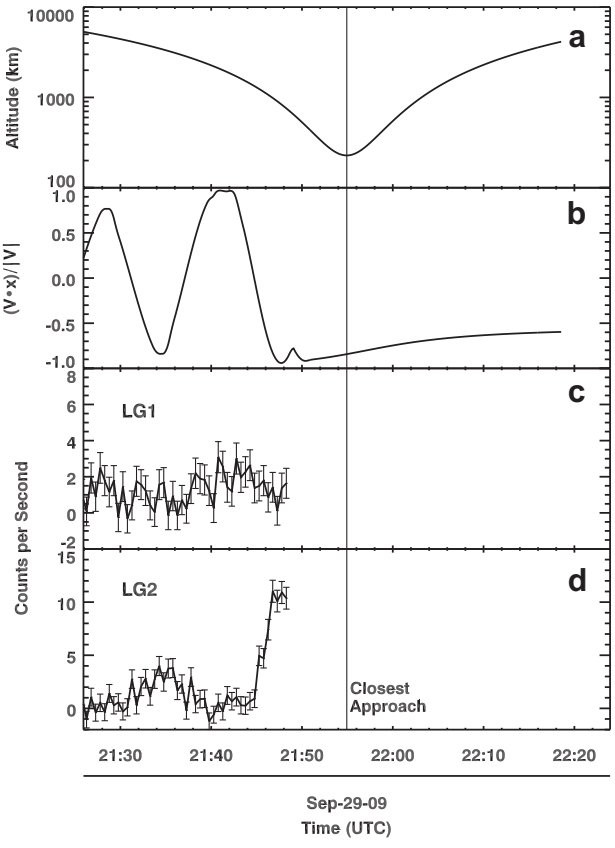

Fig. 5. MESSENGER NS data from M3. (a) Spacecraft altitude versus time. (b) $\mathbf{V}\cdot\hat{x}/|\mathbf{V}|$ versus time. (c) LG1 data in 30-s increments versus time. (d) LG2 data in 30-s increments versus time. The vertical line at 21:55 UTC denotes closest approach.

As a final step, the modeled surface neutron fluxes were analytically transformed to neutron fluxes at orbital altitude using the relations given by Feldman et al. (1989) that account for the curved neutron ballistic trajectories, gravitational binding, and finite lifetime of thermal neutrons.

4.2. Calculation of area-efficiency response

The area-efficiency response of the NS–spacecraft combination was calculated using MCNPX (Pelowitz, 2005). The NS and spacecraft were modeled with 166 cells, each of which represents a portion of a spacecraft part and/or subassembly. The most detailed part of this model was the NS, where the sensors, PMTs, Mg housing, and Gd shielding were explicitly modeled. The modeled angular response of the LG sensors matched that of pre-flight calibration data taken with the flight NS. However, we note that the absolute LG count-rate response of the NS has not yet been matched to pre-flight calibration data (Goldsten et al., 2007) because of large uncertainties in modeling the thermal neutron response of the calibration facility.

For the spacecraft, we modeled the major components expected to affect the neutron transport through the spacecraft. These include the five spacecraft fuel tanks (both the tank material and fuel), the phased-array antenna located close to the NS, the sunshade, the main spacecraft battery, the main thrusters, the carbon composite spacecraft structure, and a variety of instruments and electronics located around the spacecraft. For all electronics and sensor boxes, we used a standard electronics board composition and calculated a density that matched the volume–mass combination for each box. For some parts or groups of parts that were difficult to model in great detail (e.g., cable harnesses, fuel plumbing systems), we distributed the mass of the parts in the general vicinity of where the parts were located. For each of the flybys, we used a fuel loading appropriate to each, with a 65%, 61%, and 50% fuel loading for M1, M2, and M3, respectively. The fuel composition was hydrazine (N_2H_4) and nitrogen tetroxide (N_2O_4) (Leary et al., 2007). Due to the close proximity of the carbon composite structure to the NS, uncertainties in the construction of this structure will have the largest effect in the modeled NS response. We there-

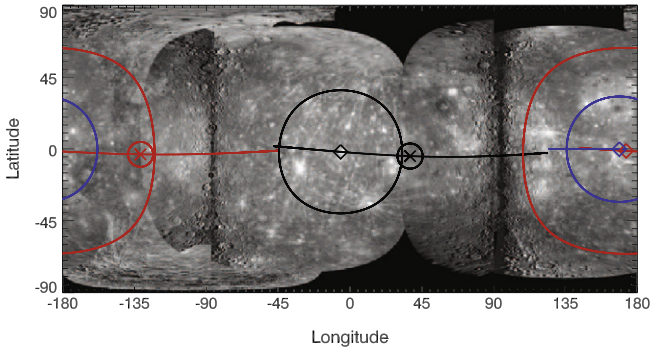

Fig. 6. Ground tracks for M1 (black), M2 (red), and M3 (blue) are superposed on a mosaic of MDIS and Mariner 10 images (B.W. Denevi, personal communication, 2009). The locations of closest approach are marked with crosses (M1 and M2 only), and the locations of LG2 thermal neutron enhancements are marked with diamonds. The approximately circular outlines around each location are the FWHM spatial footprints, which are based on spacecraft altitude (Lawrence et al., 2003; Maurice et al., 2004).

Table 1
Elemental microscopic absorption cross sections, σ_a, elemental weight fraction abundances, and thermal neutron macroscopic absorption cross section, Σ_a, for selected lunar soils.

Element	σ_a (barns)	Apollo 11	Luna 16	Luna 24	Luna 24_{Fe12}	Luna 24_{Fe10}	Luna 20	FAN
O	0.00019	0.4252	0.4203	0.4237	0.4237	0.4237	0.4401	0.4560
Na	0.528	0.0035	0.0026	0.0021	0.0021	0.0021	0.0029	0.0045
Mg	0.063	0.0478	0.0529	0.0595	0.0865	0.1115	0.0584	0.0051
Al	0.233	0.0666	0.083	0.0633	0.0633	0.0633	0.1204	0.1763
Si	0.16	0.1963	0.2074	0.2122	0.2122	0.2122	0.2113	0.2066
Ca	0.43	0.0839	0.0822	0.0791	0.0791	0.0791	0.1051	0.1359
Ti	6.11	0.0476	0.0198	0.0062	0.0062	0.0062	0.0030	0.0008
Mn	13.4	0.0016	0.0016	0.0019	0.0019	0.0019	0.0008	0.0000
Fe	2.59	0.1275	0.1302	0.1520	0.1250	0.1000	0.0580	0.0148
Sm^{144}	1.63	4.28×10^{-7}	2.57×10^{-7}	6.20×10^{-8}	0.0	0.0	9.92×10^{-8}	0.0
Sm^{147}	57	2.07×10^{-6}	1.24×10^{-6}	3.00×10^{-7}	0.0	0.0	4.80×10^{-7}	0.0
Sm^{148}	2.4	1.56×10^{-6}	9.38×10^{-7}	2.26×10^{-7}	0.0	0.0	3.62×10^{-7}	0.0
Sm^{149}	56000[a]	1.90×10^{-6}	1.15×10^{-6}	2.76×10^{-7}	0.0	0.0	4.42×10^{-7}	0.0
Sm^{150}	100	1.02×10^{-6}	6.14×10^{-7}	1.48×10^{-7}	0.0	0.0	2.37×10^{-7}	0.0
Sm^{152}	206	3.68×10^{-6}	2.22×10^{-6}	5.34×10^{-7}	0.0	0.0	8.54×10^{-7}	0.0
Sm^{154}	8.33	3.13×10^{-6}	1.88×10^{-6}	4.54×10^{-7}	0.0	0.0	7.26×10^{-7}	0.0
Sm total	–	1.38×10^{-5}	8.30×10^{-6}	2.00×10^{-6}	0.0	0.0	3.20×10^{-6}	0.0
Gd^{152}	735	3.60×10^{-8}	2.12×10^{-8}	0.0	0.0	0.0	8.80×10^{-9}	0.0
Gd^{154}	85.2	3.92×10^{-7}	2.31×10^{-7}	0.0	0.0	0.0	9.59×10^{-8}	0.0
Gd^{155}	22000[a]	2.66×10^{-6}	1.57×10^{-6}	0.0	0.0	0.0	6.51×10^{-7}	0.0
Gd^{156}	1.8	3.68×10^{-6}	2.17×10^{-6}	0.0	0.0	0.0	9.01×10^{-7}	0.0
Gd^{157}	90000[a]	2.82×10^{-6}	1.66×10^{-6}	0.0	0.0	0.0	6.89×10^{-7}	0.0
Gd^{158}	2.2	4.47×10^{-6}	2.63×10^{-6}	0.0	0.0	0.0	1.09×10^{-6}	0.0
Gd^{160}	1.41	3.94×10^{-6}	2.32×10^{-6}	0.0	0.0	0.0	9.62×10^{-7}	0.0
Gd total	–	1.80×10^{-5}	1.06×10^{-5}	0.0	0.0	0.0	4.40×10^{-6}	0.0
Σ_a	–	107.6	81.5	67.5	59.7	53.1	45.2	30.5
$\Sigma_{a(Fe,Ti,Gd,Sm)}$	–	88.3	61.1	47.7	39.6	32.6	22.4	4.7

Notes: Σ_a values are in units of 10^{-4} cm^2/g. One barn (b) = 10^{-24} cm^2. The Luna 24_{Fe10} and Luna 24_{Fe12} soils are variants of the Luna 24 soil for which Fe is set to 10 and 12.5 wt.%, respectively, and Gd and Sm abundances are set to zero. The remaining mass for these soil variants was assigned to Mg. The σ_a values were evaluated at a neutron energy of 0.025 eV and are taken from the National Nuclear Data Center (2009). Soil abundances are taken from Lawrence et al. (2006).

[a] The σ_a values for Sm^{149}, Gd^{155}, and Gd^{157} are effective averaged neutron-flux cross sections for a planetary regolith following Lingenfelter et al. (1972). $\Sigma_{a(Fe,Ti,Gd,Sm)}$ gives the combined macroscopic absorption from the strong neutron absorbers Fe, Ti, Gd, and Sm.

fore attempted to model this structure with as much precision as possible. We explicitly accounted for 15 mils of Cu grounding (Leary et al., 2007) on the structure [Cu has a large thermal neutron-absorption cross section of 4.47 barns (b)]. The carbon composite structure consists of two face plates covering an irregular ribbed structure. Because the ribbed structure is too fine and variable in scale across the spacecraft to model explicitly, a combination of spacecraft drawings and empirical pre-launch measurements was used to determine that the carbon composite density was 0.32 ± 0.03 g/cm^3. The composition of the carbon composite structure is 70% carbon (fiber) plus 30% cyanate ester epoxy resin. In summary, our modeled spacecraft dry mass is 504 kg, which is within less than 1% of the final spacecraft dry mass of 508 kg (Leary et al., 2007). Calculations made with spacecraft models having somewhat different total dry mass indicate that such a small difference in mass has a negligible effect on the overall NS response.

To obtain the area-efficiency response of the LG sensors, the entire spacecraft was illuminated with plane-wave neutrons having 31 different energies (10^{-9}–10 MeV) and 104 different azimuth and elevation angle combinations. For each energy, the modeled angular response was interpolated over a sphere to create the final response function grid on 5° × 5° grid points. Fig. 7 shows maps of this response for three different neutron energies. For low-energy neutrons (0.0066 eV) for which the intrinsic efficiency of the LG scintillators is near 100%, the modeled effective area is close to 100 cm^2, which is the physical area of each scintillator. For LG1, the effect of the phased-array antenna that lies within the LG1 field of view is seen around 10° horizontal, 45° vertical. For medium-energy neutrons (10 keV), the response is smoother and more diffuse because the higher-energy neutrons are more penetrating and not as attenuated by the spacecraft material. Finally, for high-energy neutrons (10 MeV), there is a general diffuse response, which is likely due to the spacecraft material having less attenuation, as well as the down-scatter of higher-energy neutrons to lower energies where they are more efficiently detected with the LG sensors.

4.3. Calculation of modeled Neutron Spectrometer counting rate

After determining the orbital neutron flux and the NS neutron response, the modeled counting rate integral in Eq. (1) was calculated by numerical integration from thermal energies up to 10 MeV. For test functions that are analytically integrable, the numerical technique reproduced the analytic integral to within a few percent. The integral of Eq. (1) was calculated for different time steps along the flyby trajectory. Spacecraft ephemeris and orientation information was used with angular transformations that properly account for angular dependencies of $\mathbf{V}_T \cdot \hat{n}/|\mathbf{V}|$, $\varepsilon(\varphi_D, \mu_D, K_D)$, and $\Phi(\varphi, \mu, K)$. A normalization factor, $N = N_{GCR} N_{MCNPX} N_M$, was applied to the model. N_{GCR} is the factor of 6.4 GCR protons cm^{-2} s^{-1} discussed above. $N_{MCNPX} = 1/4$ was applied to account for factors specific to the MCNPX Mercury flux model (McKinney et al., 2006). The remaining normalization, N_M, was determined by fitting the measured LG1 and LG2 data to the model as is described in the next section. Appendix B describes the procedure that was used to validate this model using relatively well-understood data from the Neutron Spectrometer on Lunar Prospector (Maurice et al., 2004).

5. Results of Neutron Spectrometer transport model

To account for variations due to both normalization and soil composition, χ^2 values were calculated from both LG1 and LG2

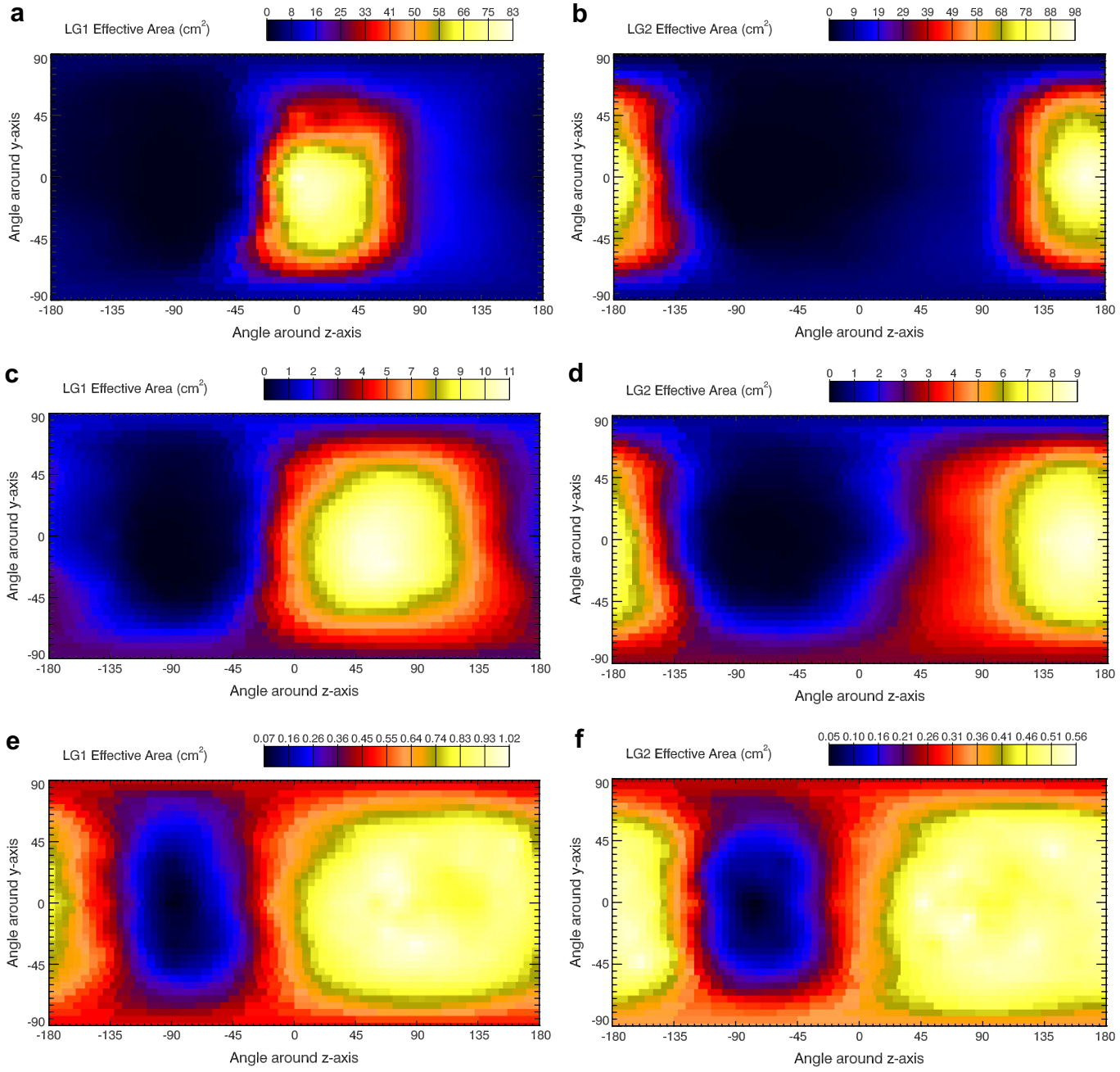

Fig. 7. Maps of the LG response in units of effective area (cm^2). The center of the map is the response for an incoming direction corresponding to the spacecraft *x*-axis. Horizontal angles correspond to angles measured anticlockwise around the spacecraft *z*-axis starting from 0°; vertical angles correspond to angles measured anticlockwise around the spacecraft *y*-axis starting from 0°. (a), (c), and (e) show the LG1 response and (b), (d), and (f) show the LG2 response. (a) and (b) show the response for low neutron energies (0.0066 eV), (c) and (d) show the response for medium neutron energies (10 keV), and (e) and (f) show the response for high neutron energies (10 MeV).

data in a manner so that parameters for composition (Σ_a) and normalization (N_M) were allowed to vary:

$$\chi^2(N_M, \Sigma_a) = \sum_{j=0}^{1} \frac{\sum_{i=0}^{n} w_{i,j} \left(\frac{M_{i,j}(N_M, \Sigma_a) - d_{i,j}}{\sigma_{i,j}} \right)^2}{\sum_{i=0}^{n} w_{i,j}}, \quad (2)$$

$d_{i,j}$, $M_{i,j}$, and $\sigma_{i,j}$ are data, model, and uncertainty values for the n time measurements i. The indices $j = 0$ and 1 represent measurements from LG1 and LG2, respectively. $w_{i,j}$ are weighting factors that account for the fact that some data points are more sensitive to model variations (e.g., data points near the thermal enhancement peak or CA peak) than other data points and we want the fit to explicitly take this sensitivity into account by setting $w_{i,0} = d_{i,0}/\max(d_{i,0})$ (and similarly for the $j = 1$ index). To find the minimum χ^2 value, and hence the best fit of the model to the data, N_M values were varied from 0.7 to 1.3, and the soil compositions were varied among the soils listed in Table 1.

Results of applying the χ^2 minimization procedure to M1 data are shown in Table 2. For each soil, the N_M value with the minimum χ^2 value is shown along with the corresponding χ^2_{min} value. The overall minimum χ^2 value of $\chi^2_{min} = 1.69$ is found for a Luna 24_{Fe12} soil ($\Sigma_a = 59.7 \times 10^{-4}$ cm^2/g). The corresponding best-fit normalization constant is $N_M = 1.07$, which is within the acceptable uncertainties given the model's validation with Lunar Prospector data (Appendix B). Fig. 8 shows the best-fit time-dependent count

Table 2
Best-fit N_M and χ^2_{min} values for a given soil composition from the combined fitting of M1 LG1 and LG2 data to the count rate model.

Composition	N_M	χ^2_{min}
Apollo 11	1.13	3.89
Luna 16	1.10	2.48
Luna 24	1.09	1.87
Luna 24_{Fe12}	1.07	1.69
Luna 24_{Fe10}	1.05	1.82
Luna 20	1.01	2.41
FAN	0.88	6.32

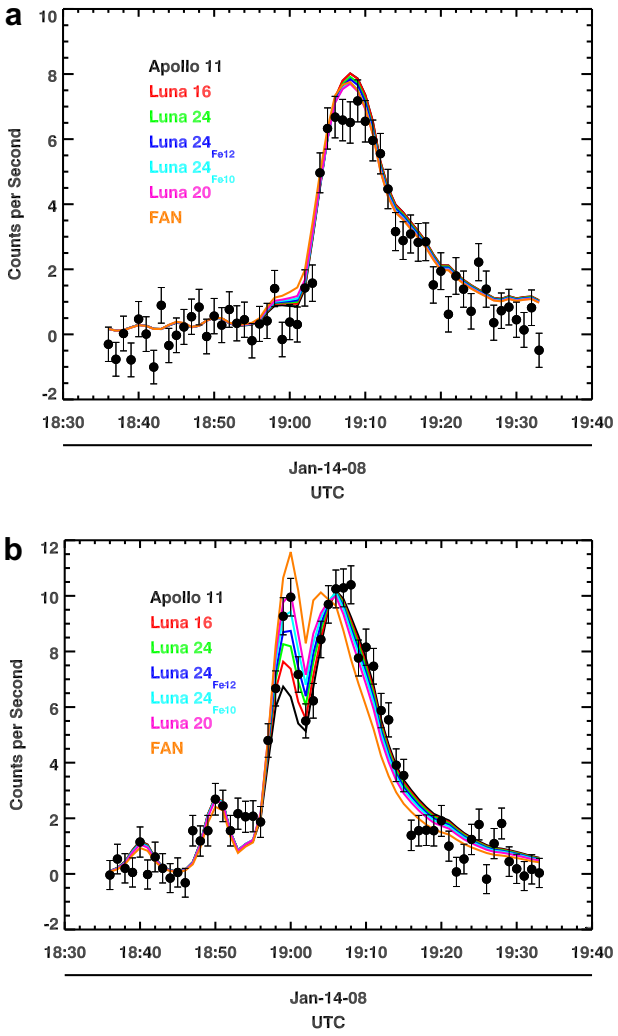

Fig. 8. (a) LG1 and (b) LG2 time-series data from Fig. 3c and d for M1 compared with modeled counting rates for different soil compositions. The different compositions are FAN (orange), Luna 20 (pink), Luna 24_{Fe10} (light blue), Luna 24_{Fe12} (blue), Luna 24 (green), Luna 16 (red), and Apollo 11 (black).

rates for LG1 and LG2 data. For LG1 (Fig. 8a), the modeled count rates for all soils are shown with the overall best-fit normalization parameter of 1.07. A good fit is seen, as the model is within one standard deviation for all but a few data points; the remaining data points are within two standard deviations. Fig. 8b shows the best-fit models for LG2 data using the N_M parameters listed in Table 2. As seen, the thermal enhancement and main peaks, as well as the valley between the two peaks, all must be fit to obtain an acceptable overall fit.

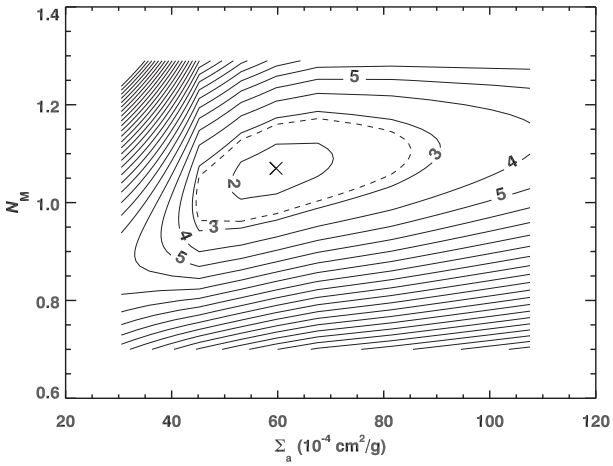

Fig. 9. Contours of χ^2 values for the fit of M1 data to the modeled count rates for variations in N_M and Σ_a. The minimum χ^2 is shown by a cross. The $\chi^2_{min}+1$ contour is shown by a dashed line.

An informative way to understand the fit uncertainties is to plot χ^2 contours for the range of N_M and Σ_a parameters (Fig. 9). Here the clear minimum is seen for $\Sigma_a = 60 \times 10^{-4}$ cm^2/g and $N_M = 1.07$. The $\chi^2_{min}+1$ contour is shown by the dashed line. With the assumption that all the uncertainties are due to Poisson counting statistics, there is a statistical likelihood of 68% that the LG1 and LG2 data are described by a parameter combination that lies within the $\chi^2_{min}+1$ contour. For the N_M values, this result implies that acceptable values range from 0.95 to 1.15, which is within the uncertainty suggested by the Lunar Prospector validation described in Appendix B. Acceptable values of Σ_a range from 45 to 85×10^{-4} cm^2/g.

This analysis is premised on a uniform composition for the entire region measured by the NS, but this assumption may not be valid. To illustrate, Fig. 6 shows the FWHM NS footprint for the thermal neutron enhancement and closest approach (black trace with a diamond and cross, respectively). On a scale of 0–255, the average albedo for the thermal neutron enhancement is 162 and for closest approach the average albedo is 143, which is a ~12% difference. The lower albedo at closest approach suggests that this region may have a larger concentration of optical darkening agents such as the neutron absorbers Fe and Ti. If this is the case, then the NS data at the thermal neutron enhancement could be better fit by an average composition closer to Luna 24_{Fe10} ($\Sigma_a = 53 \times 10^{-4}$ cm^2/g), and later in the encounter by a more highly neutron absorbing soil, such as Luna 16 ($\Sigma_a = 81 \times 10^{-4}$ cm^2/g) to provide a better fit to the valley and closest-approach peak. Nevertheless, adding additional parameters to the model (i.e., non-uniform composition) appears to be unwarranted at the current stage of data acquisition and analysis. Therefore, our assumption of uniform composition provides a best estimate for the average composition over the surface region measured with NS data. Once MESSENGER is in orbit about Mercury, the question of non-uniform composition on Mercury's surface will be addressed by global measurements with the NS as well as MESSENGER's Gamma-Ray Spectrometer and X-Ray Spectrometer.

Systematic uncertainties in the model count rates may also be reduced by a refinement of the NS response model. For example, as noted in Section 4, the density of the carbon composite spacecraft structure is uncertain by as much as 10%. In other determinations of a spacecraft model, we found that variations in the density of the carbon composite material by ±50% could alter the best-fit soil type by ~20×10^{-4} cm^2/g. Because the uncertainty in the density of the carbon composite material is only 10%, we conclude that

this uncertainty in carbon composite density, although it translates into some uncertainty in the best-fit soil type, will not likely affect our overall conclusions.

The χ^2 minimization procedure used for M1 can also be used for M2 and M3 data. Model fits and χ^2 contours for M2 and M3 data are shown in Figs. 10–13 and Tables 3 and 4. With this minimization procedure, neither dataset is able to provide definitive conclusions about the surface abundance of neutron-absorbing elements. For M2, the spacecraft rotation that provides the thermal neutron Doppler enhancement occurred too far from Mercury to give an enhancement peak that discriminates among soil compositions. As a consequence, all soils provide an acceptable fit, as is shown by the lack of a clear minimum in χ^2 in Fig. 11. The M2 data do show a stable normalization constant of $N_M = 1.00–1.02$, which demonstrates that the model is accurately calculating the absolute count rate.

For M3, the lack of a strong peak at closest approach prevents a good determination of N_M in the two-parameter minimization procedure, which results in an inability to determine a clear χ^2_{min} value within the range of fitted N_M and Σ_a values (Fig. 13). However, Wiedenbeck et al. (2009) showed that the GCR solar modulation parameter changed sufficiently from January 2008 to mid-2009 to result in a GCR flux that is at least 10% higher for the M3 mea-

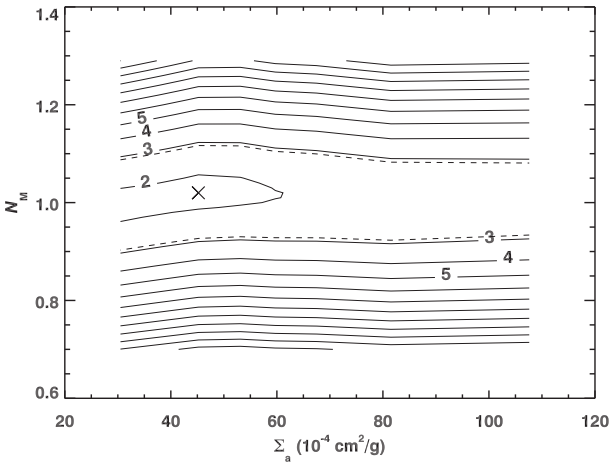

Fig. 11. Contours of χ^2 values for the fit of M2 data to the modeled count rates for variations in N_M and Σ_a. The minimum χ^2 is shown by a cross. The $\chi^2_{min} + 1$ contour is shown by a dashed line.

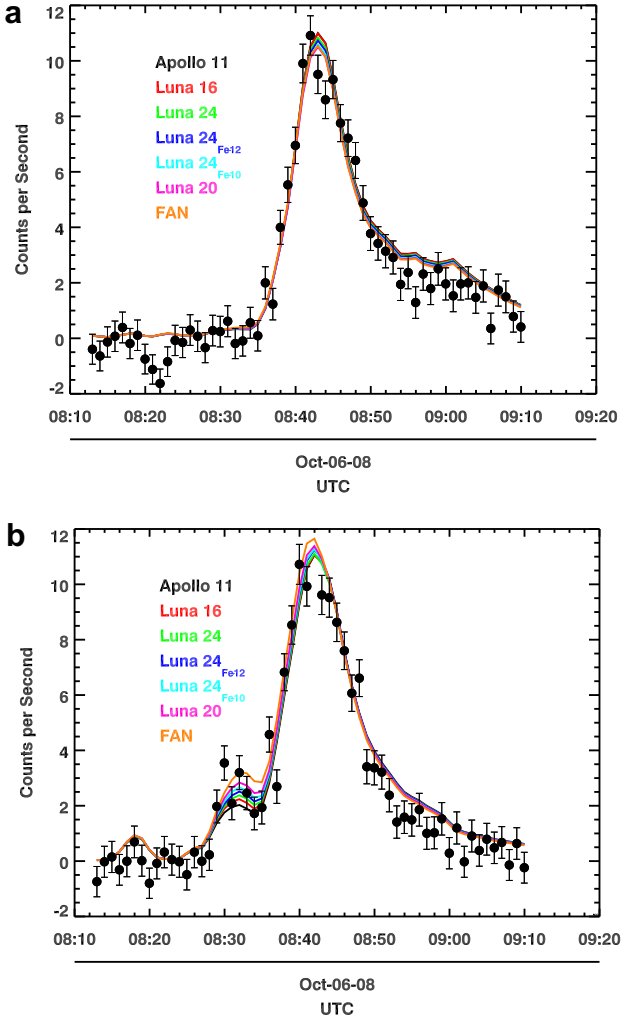

Fig. 10. (a) LG1 and (b) LG2 time-series data from Fig. 4c and d for M2 compared with modeled counting rates for different soil compositions. The different compositions are FAN (orange), Luna 20 (pink), Luna 24$_{Fe10}$ (light blue), Luna 24$_{Fe12}$ (blue), Luna 24 (green), Luna 16 (red), and Apollo 11 (black).

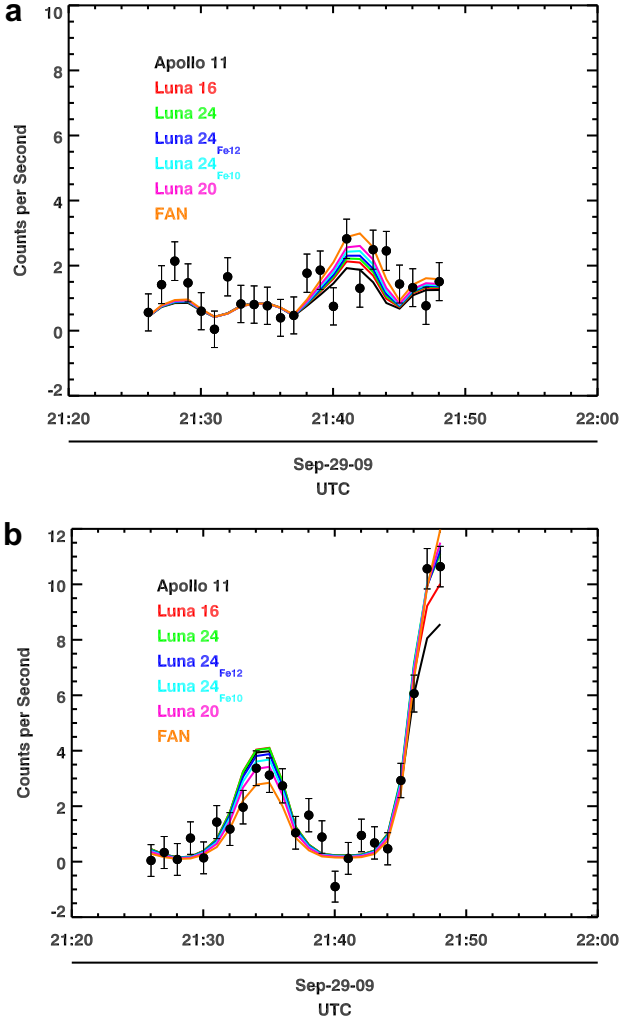

Fig. 12. (a) LG1 and (b) LG2 time-series data from Fig. 5c and d for M3 compared with modeled counting rates for different soil compositions. The different compositions are FAN (orange), Luna 20 (pink), Luna 24$_{Fe10}$ (light blue), Luna 24$_{Fe12}$ (blue), Luna 24 (green), Luna 16 (red), and Apollo 11 (black).

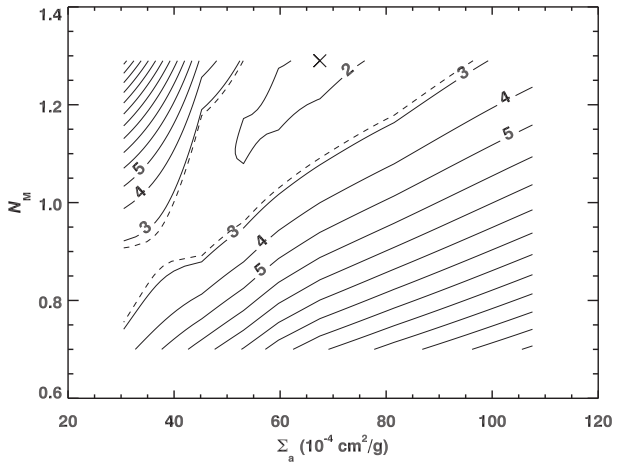

Fig. 13. Contours of χ^2 values for the fit of M3 data to the modeled count rates for variations in N_M and Σ_a. The minimum χ^2 is shown by a cross. The $\chi^2_{min}+1$ contour is shown by a dashed line.

Table 3
Best-fit N_M and χ^2_{min} values for a given soil composition from the combined fitting of M2 LG1 and LG2 data to the count rate model.

Composition	N_M	χ^2_{min}
Apollo 11	1.01	2.25
Luna 16	1.00	2.13
Luna 24	1.01	2.04
Luna 24_{Fe12}	1.02	1.99
Luna 24_{Fe10}	1.02	1.91
Luna 20	1.02	1.86
FAN	1.01	1.87

Table 4
Best-fit N_M and χ^2_{min} values for a given soil composition from the combined fitting of M3 LG1 and LG2 data to the count rate model.

Composition	N_M	χ^2_{min}
Apollo 11	1.29	3.43
Luna 16	1.29	2.10
Luna 24	1.29	1.85
Luna 24_{Fe12}	1.21	1.88
Luna 24_{Fe10}	1.13	1.93
Luna 20	1.03	2.03
FAN	0.83	2.50

surement. If this information is used to independently set the N_M value for M3 as $N_{M,M3} = 1.07 \times 1.10 = 1.17$, then Table 4 broadly suggests that a Luna 24_{Fe12} soil (with a best-fit $N_M = 1.21$) is the best match to the M3 data, which is consistent with the M1 results.

In summary, these results show that NS data from M1 are best fit by a neutron-equivalent-absorbing composition ranging from Luna 24_{Fe12} to Luna 16 ($\Sigma_a = 45$–81 cm^2/g). With the two-parameter, two-sensor fit, M2 and M3 data cannot provide sufficient discrimination to reliably measure Mercury's surface composition, but when independent information on GCR flux is used, the M3 data are shown to be consistent with those of M1. Further, we cannot rule out the possibility that the portion of Mercury's surface measured with M1 neutron data has a non-uniform composition. Finally, the good agreement between the neutron transport model and absolute and time-dependent relative counting rates give us confidence that the overall neutron count rate model is fundamentally sound.

6. Discussion and conclusions

The analysis of the NS data presented here provides new information about Mercury's surface composition. In particular, we conclude that Mercury's surface composition is not similar to regions of the lunar highlands having low abundances of Fe, Ti, Gd, and Sm (e.g., FAN). This result is markedly different from an earlier conclusion from a preliminary analysis of M1 NS data that Mercury's surface has a neutron absorption consistent with less than 6 wt.% Fe (Solomon et al., 2008). The reason for this change in conclusions is that the earlier results did not fully take into account effects on neutron measurements of the MESSENGER spacecraft, which have been explicitly modeled in this study.

With this measured Σ_a, we can make direct comparisons with modeled estimates of Mercury's surface composition. Taylor and Scott (2003) provided estimated compositions for three different models: a refractory-volatile mixture model (Morgan and Anders, 1980), a metal-rich chondrite model, and a partial melt composition based on an enstatite chondrite bulk composition (McCoy et al., 1999). The Σ_a values for these models are $\Sigma_a = 39 \times 10^{-4}$, 34×10^{-4}, and 22×10^{-4} cm^2/g, respectively. Our measurements of Σ_a rule out the metal-rich chondrite and enstatite chondrite, and most likely the refractory-volatile mixture model (see Fig. 14). We also note that there are other model estimates of the composition of Mercury's mantle plus crust (e.g., Goettel, 1988; Lodders and Fegley, 1998). Although those estimates are not directly applicable to Mercury's surface composition, the Σ_a values for all these models are low compared to our measured value of Σ_a because of the low model concentrations of neutron-absorbing elements.

We further conclude that the likely neutron-absorbing elements on Mercury's surface are Fe, Ti, Gd, and/or Sm. The reason for this conclusion is twofold. First, for all ranges of lunar soil compositions, the contribution of Fe, Ti, Gd, and Sm to the total Σ_a varies by almost a factor of 19 (4.7–88×10^{-4} cm^2/g) compared to a variation of 1.35 (19.1–23.5×10^{-4} cm^2/g) from the combination of all other elements. Thus, Fe, Ti, Gd, and Sm almost completely determine the total neutron absorption of these types of non-hydrated silicate compositions. Second, although other elements do have microscopic absorption cross sections as high or higher than Fe and Ti (2.59 b and 6.11 b, respectively), such as ^{35}Cl ($\sigma_a = 44$ b), ^{63}Cu ($\sigma_a = 4.47$ b), ^{55}Mn ($\sigma_a = 13.4$ b), and ^{58}Ni ($\sigma_a = 4.6$ b), it is not expected in non-hydrated, silicate planetary materials that

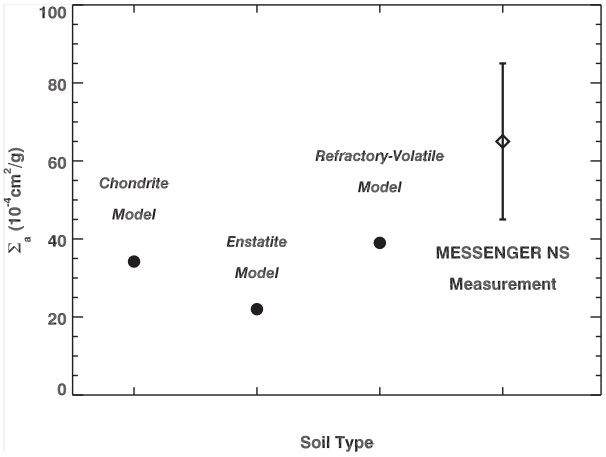

Fig. 14. Summary of the macroscopic neutron-absorption cross sections, Σ_a, for modeled Mercury soils from Taylor and Scott (2003) (closed circles), compared with the measured MESSENGER NS data (diamond) and the 1-σ error in the model fit to the data (error bar).

the abundances of these or other such elements would be as high as the few weight percent required to measurably affect Σ_a. For example, 4–5 wt.% of MnO, which has the largest σ_a of the other elements listed above, is required in the model compositions of Taylor and Scott (2003) to increase Σ_a to the medium range of our measured Σ_a values, but such an abundance would be almost two orders of magnitude larger than the values given by Taylor and Scott (2003). While such high values of Mn (and other similar elements) cannot be completely ruled out, they are unlikely to apply to large parts of Mercury's surface. Thus, we conclude that some combination of Fe, Ti, Gd, and Sm are driving the measured neutron absorption on Mercury. We also note that during MESSENGER's orbital mission, the Gamma-Ray and X-Ray Spectrometers will provide complementary measurements of Fe and Ti, so that the assertion that Fe, Ti, Gd, and Sm are the dominant neutron absorbers will be independently testable.

Our results are consistent with the inference of Denevi et al. (2009) that Mercury's color variations and visible and near-infrared reflectance spectra may indicate substantial amounts of Fe–Ti oxides (e.g., ilmenite) on Mercury's surface. If the dominant sources of neutron absorption are Fe–Ti oxides, then the crust of Mercury may indeed have abundant Fe, even if not present to a measurable degree as FeO in silicate minerals. Thus, the non-detection of the 1-μm absorption feature in Mercury's surface does not require a low total Fe abundance. Moreover, we may compare the NS results quantitatively to the determination of Denevi et al. (2009) that Mercury's intermediate terrain (IT), the dominant terrain type in the area of the thermal enhancement peak during M1 (2.5°S, 357°E), may have up to 15% ilmenite by volume, which we take to be equivalent to 22 wt.% ilmenite under the assumption of a crustal density of 3 g/cm^3 (Lodders and Fegley, 1998) and an ilmenite density of 4.8 g/cm^3. To make this comparison, we assume for simplicity that all the observed neutron absorption from Fe, Ti, Gd, and Sm is caused solely by Fe and Ti in ilmenite, or:

$$\Sigma_{a,\mathrm{Ilmenite}} = \frac{f_{\mathrm{Ilmenite}}(\sigma_{\mathrm{Fe}} + \sigma_{\mathrm{Ti}})N_A}{A_{\mathrm{Ilmenite}}} = \sum_{i=\mathrm{Fe,Ti,Gd,Sm}} \frac{f_i \sigma_i N_A}{A_i}. \quad (3)$$

Solving for f_{Ilmenite} and using $\Sigma_{a(\mathrm{Fe,Ti,Gd,Sm})}$ values (see Table 1) in the range $(22\text{–}61) \times 10^{-4}$ cm^2/g, we find f_{Ilmenite} = 7–18 wt.%. The upper reach of this range is consistent with values for IT inferred from color and reflectance. We note, finally, that if Gd and Sm abundances on Mercury's surface are as high as tens of parts per million, then the Fe and Ti abundances will be lower than the values given above.

We cannot rule out the presence of metallic iron on Mercury's surface, but because metallic iron is not particularly low in reflectance, and because it has a fairly steep or "red" slope to its reflectance spectrum (e.g., Cloutis et al., 2010), it is not likely to be the primary darkening agent on Mercury or to be responsible for the lower spectral reflectance and shallower spectral slope in areas of low-reflectance material (Denevi et al., 2009). The implication of these arguments is that Fe^{2+} is likely to be present on the surface of Mercury but primarily in non-silicate phases. This inference contrasts sharply with the presumption that the large metallic core and absence of Fe^{2+} in crustal silicates on Mercury resulted from formation at very low oxygen fugacity.

Knowledge of the crystallization behavior of lunar rocks as a function of oxygen fugacity may provide guidance on this last issue. Usselman and Lofgren (1976) demonstrated that between the iron–wüstite (IW) buffer and one log unit below IW, Ti-rich mare basalts crystallize ilmenite prior to the dominant mafic silicate, pyroxene. If basalts on Mercury contain a higher TiO_2/FeO ratio than their lunar counterparts, early crystallizing ilmenite might effectively remove all FeO from the melt, leaving very FeO-poor pyroxene. This conclusion would imply that the oxygen fugacity of basalts on Mercury is at the upper range of oxygen fugacities derived for the Moon (IW to IW-2; Wadhwa, 2008).

Acknowledgments

The first author thanks Dorthea Delapp of Los Alamos National Laboratory for early help in the data reduction of MESSENGER NS data and acknowledges support from the MESSENGER Participating Scientist Program. Thorough suggestions by Richard Elphic and an anonymous reviewer greatly improved this paper. We thank Miriam Riner for pointing out a need to clarify the discussion in the text on the application of Eq. (3). The MESSENGER project is supported by the NASA Discovery Program under contracts NASW-00002 to the Carnegie Institution of Washington and NAS5-97271 to the Johns Hopkins University Applied Physics Laboratory.

Appendix A. Details of the data reduction process

In this appendix, we describe the process for determining the net counting rates from the LG1 and LG2 sensors. The steps that we use are to (1) determine an appropriate background counting rate to subtract from the flyby data and (2) verify the background subtraction by fitting the background-subtracted spectra with a Gaussian function for different conditions. We then demonstrate that the fit provides adequate residuals and show the time-series counting rate for different fit and spectral summing conditions that minimize the contribution from background gamma-rays.

A.1. Background subtraction

As described in the main text, the background spectra were chosen to be the average, one-day spectra taken both before and after closest approach (CA). Fig. A1 shows the LG1 and LG2 background spectra (red traces) along with the CA spectra (black traces) within ±5 min of CA from the M1 flyby. The background-subtracted net spectra are shown as the blue histograms in Fig. A1. The net spectra consist mainly of counts from the ^{6}Li(n,α)^{3}H reaction in the Li glass sensors along with some residual background counts at low channels that are likely due to gamma-rays from Mercury's surface.

A.2. Fitting the net spectra

The net spectra in Fig. A1 were well fit by a full Gaussian function above channel 17 (blue traces). The width of this peak (23%) has a similar magnitude to the width (~25%) seen in pre-launch calibration data (Goldsten et al., 2007). Since we have verified that the peak width and position remain constant throughout the flyby, we can determine total net counting rates using a fitting procedure that fixes the width and position to values shown in Fig. A1 and allowing only the amplitude to vary. An example of this "amplitude-only" fit is shown by the dashed orange trace in Fig. A1. As expected, it lines up very closely with the full fit.

A good check on the goodness of a fit is obtained by looking at the fit residuals, or the difference between the fit and the data. Fig. A2 shows the residuals for the LG1 and LG2 fits. Except for the region at channels ~5–12 with positive values, the residuals are consistent with zero, which indicates a good fit. We are, however, concerned about how these low channel background counts may affect the overall determination of total net counts. To assess this possible effect, Figs. A3 and A4 show LG1 and LG2 spectra for two different 2-min periods, one period around CA and one period around the thermal neutron enhancement peak at 18:59 UTC. The amplitude of the net spectra is fit with a Gaussian function having the same width and position as the Gaussian peaks in Fig. A1. For the CA data, the low channel background is present in both LG1

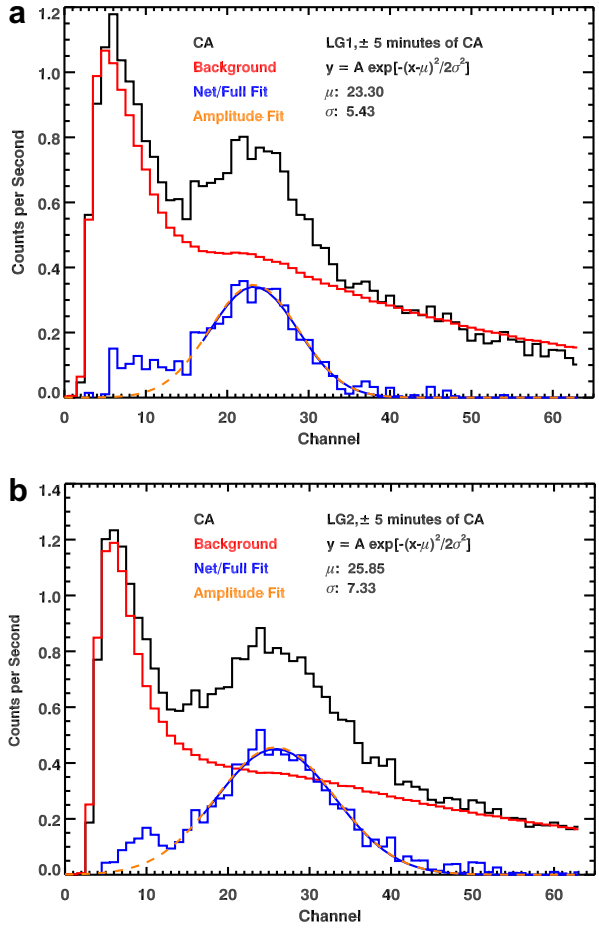

Fig. A1. M1 pulse-height data from the (a) LG1 and (b) LG2 sensors. Data taken within 5 min of CA are shown by the black trace. Background data are shown in the red trace. Background-subtracted (net) data and a Gaussian fit to the background-subtracted data are shown in blue. An amplitude-only fit to the net spectra is shown in the dashed orange. The fit parameters for the full Gaussian fit are indicated on each figure.

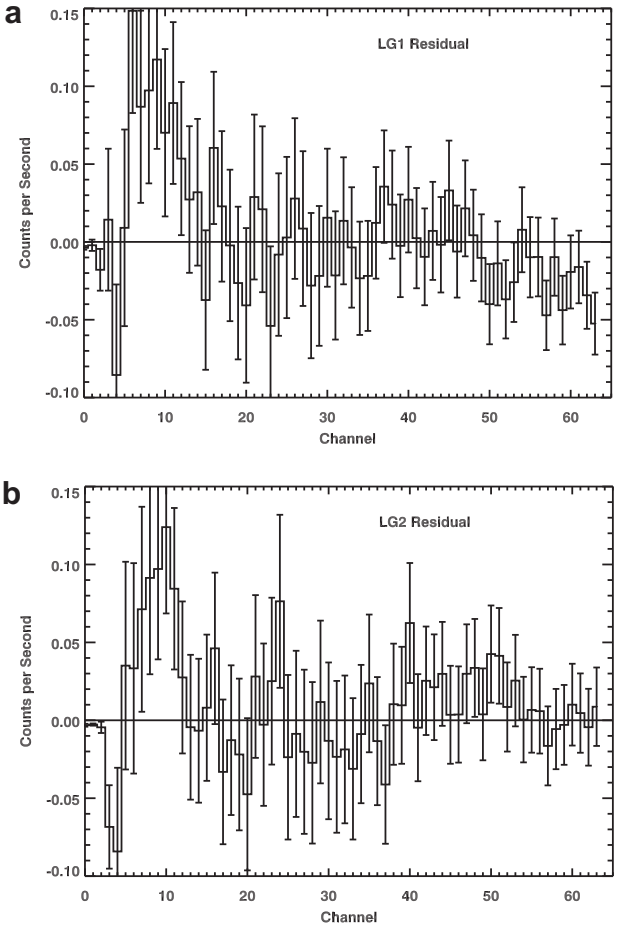

Fig. A2. Residuals (net spectra minus fit from Fig. A1) for the (a) LG1 and (b) LG2 sensors.

and LG2 sensors. For the thermal enhancement peak data, there is no low channel background in LG1 or LG2, even though there are substantial neutron counts for LG2 due to the thermal neutron enhancement peak. This result is consistent with the idea that these background counts are gamma-rays from Mercury, which would have larger fluxes at a CA altitude of ~200 km than at 18:59 UTC, where the altitude was ~900 km. In addition, if these background counts could affect the total net count values, this effect will be more clearly seen for CA data, where the background counts are present.

To further assess how the low channel background affects the total net count values, Fig. A5 shows LG2 time series total counting rates for different fitting or summing conditions. For lines labeled "thresh" (solid black, red, blue, and orange lines), the total net counts are the total counts above the given channel threshold. These counts have been normalized by

$$N = \frac{\sum_{i=0}^{D_{\text{Total}}} g_i}{\sum_{i=D_{\text{thresh}}}^{D_{\text{Total}}} g_i}, \tag{A1}$$

where g_i is the Gaussian function from Fig. A1, D_{Total} is the total number of channels, and D_{thresh} is the threshold channel.

The black dashed line shows the results when the total net counts are determined by summing the amplitude-fitted Gaussian function. Finally, the green trace shows the result when the total spectra are smoothed over 60 s. The uncertainties for the summed counts above a threshold are assumed to follow a Poisson distribution and are calculated using

$$\sigma = \sqrt{\frac{C}{N\tau} + \frac{C_{\text{back}}}{N_{\text{back}}\tau_{\text{back}}}}, \tag{A2}$$

where C is the total counting rate (black trace in Fig. A1), $N = 30$ is the number of 2-s measurements in each data point, C_{back} is the background counting rate, N_{back} is the total number of measurements averaged in the background data, and τ and τ_{back} are the accumulation times per measurement.

These results show that there is little variation in the thermal enhancement peak for the different methods of determining the total net counts. However, there is a noticeable difference for the CA peak in that the smoothed and low-threshold determinations show higher relative counts than the high-threshold and fitted values. Therefore, the gamma-ray background can affect the determination of neutron-absorbing elements if it is not properly treated, because the abundances of such elements effectively depend on the relative heights of the CA and thermal enhancement peaks.

To ensure that any effect from this low channel background is minimized, we have chosen to calculate the total net counts by summing the net spectra above a threshold value of 17. The total net counts are further normalized using Eq. (A1), and the uncertainties are calculated using Eq. (A2).

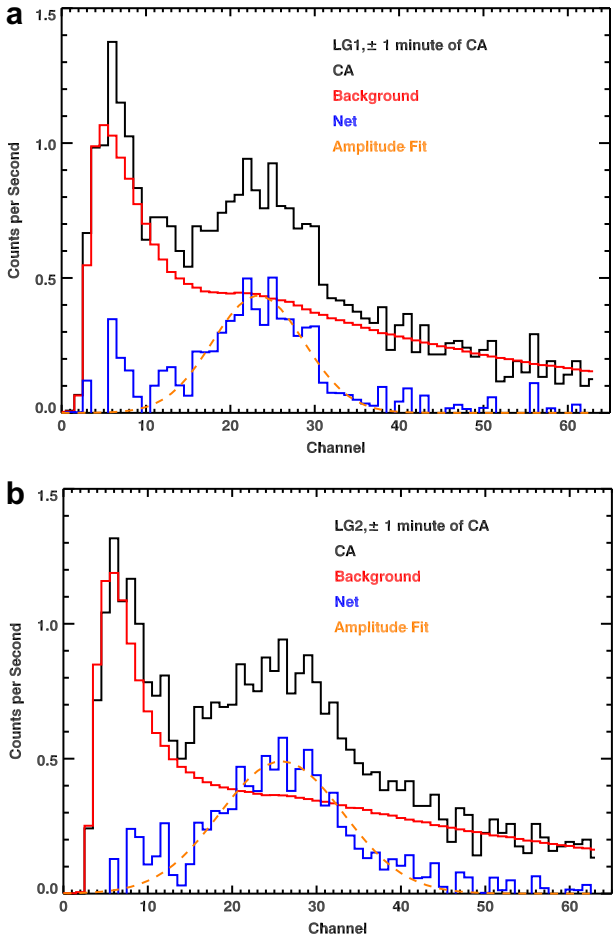

Fig. A3. Comparison of M1 pulse-height data from the (a) LG1 and (b) LG2 sensors taken within 1 min of CA (black trace) with background data (red trace). Background-subtracted (net) data are in blue. An amplitude-only fit to the net spectra is shown in the dashed orange.

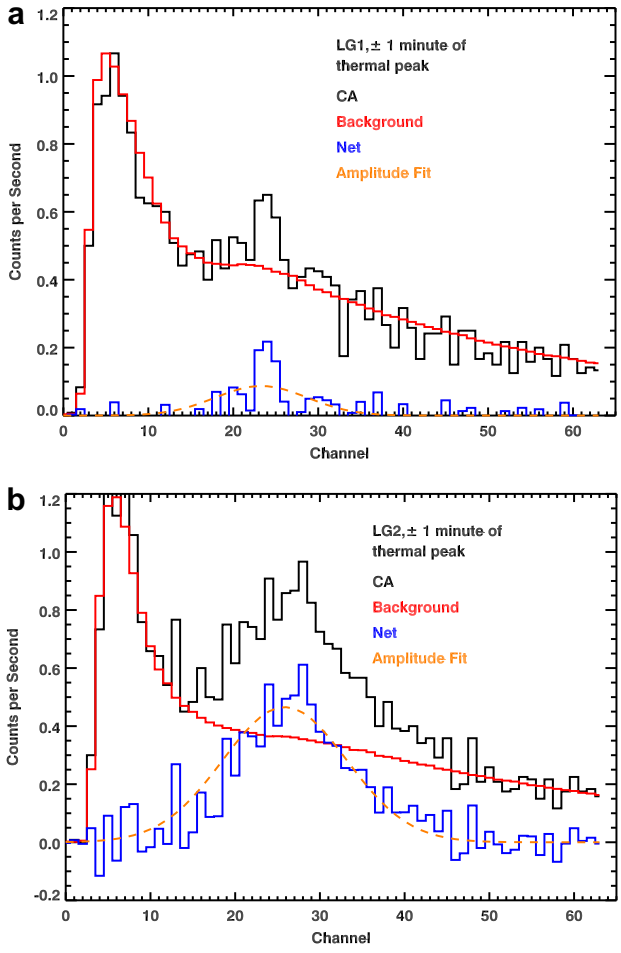

Fig. A4. Comparison of M1 pulse-height data from the (a) LG1 and (b) LG2 sensors taken from within 1 min of the thermal enhancement peak (black trace) with background data (red trace). Background-subtracted (net) data are in blue. An amplitude-only fit to the net spectra is shown in dashed orange.

Appendix B. Validation of the neutron transport model

Validating the neutron transport model is an important step toward developing confidence in the model's ability to predict neutron counting rates and ultimately Mercury's surface composition. One part of model validation concerns the measured and modeled relative counting rates. Figs. 8, 10 and 12 of Section 5 demonstrate that given an appropriate soil composition and known instrument and spacecraft composition, the relative modeled counting rates show a very good correspondence to the measured data. Even so, iterations in the model have shown that variations in the spacecraft composition and density can translate into differences in the final results. Thus, as the orbital mission proceeds and more neutron data are measured, we expect that refinements may be made to the modeled response.

A second part of model validation concerns an accurate prediction of absolute counting rates. One of the major factors that influences the absolute counting rate is the absolute GCR flux, which can vary by more than a factor of two between solar minimum and solar maximum. Historically, a source of significant uncertainty has been how the GCR protons and alpha particles are converted into neutrons via various high-energy physics interactions (McKinney et al., 2006). In response to these uncertainties, McKinney et al. (2006) carried out a benchmark study of MCNPX with Apollo 17 drill core neutron measurements. With appropriate input parameters, McKinney et al. (2006) were able to validate the GCR-to-thermal-neutron physics models to better than 10%, thus significantly reducing a major source of prior uncertainties. Lawrence et al. (2006) carried out a model validation of MCNPX with Lunar Prospector (LP) Neutron Spectrometer (NS) data and found that the model could reproduce the data to better than 10% for thermal and epithermal neutrons.

Building on that prior work, the validation described here again uses LP–NS data as a validation dataset. In addition to a significantly revised implementation of Eq. (1) that has been fully generalized to accept neutron fluxes from any planet, any energy range, any instrument orientation, and any set of spacecraft orbital parameters, this new validation uses revised GCR and LP–NS input parameters. LP–NS data are ideal to use as a validation dataset for several reasons. First, ^{3}He neutron sensors in general, and the LP-NS ^{3}He sensors in particular are well studied and well understood. Second, the LP-NS sensors were mounted on the end of a 2.5-m boom, and effects from spacecraft-generated background neutrons were minimized. Third, the soil composition of the lunar highlands, which is the general region used for validation, is well known (Prettyman et al., 2006). Therefore, uncertainties from surface composition assumptions are minimized. This validation will be described in two parts. First, the integrand for both LP and MESSENGER will be investigated to understand the differences between the two neutron instruments. Second, the modeled count rate will be calculated for the LP NS and compared to measured data.

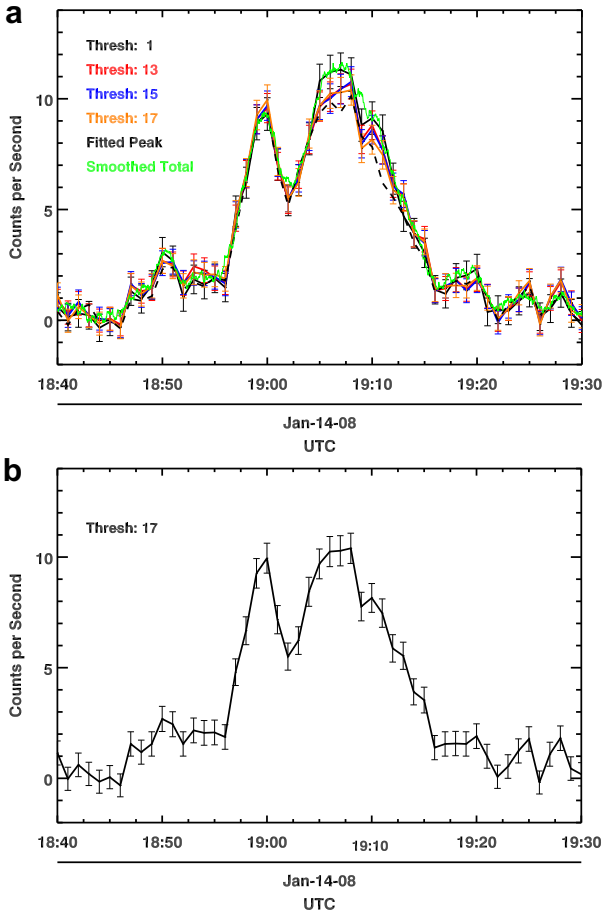

Fig. A5. (a) Time-series counting-rate data determined for various methods (counts above threshold, peak fitting, and smoothing of total counts) and (b) time-series counting-rate data for the counts above the threshold value of 17. Data are from the M1 flyby.

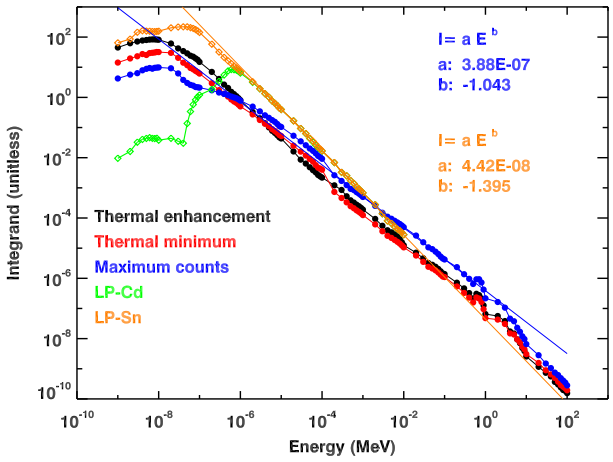

Fig. B1. Plot of angle-integrated integrand of Eq. (1) for three different time steps of MESSENGER M1 data using a Luna 24 soil (black, red, blue), and for the two LP sensors for a FAN-type soil. Power laws fit to the upper portions of the blue and orange traces are shown by the straight solid lines. The power-law fit parameters are shown at the upper right.

The angle-integrated integrand of Eq. (1) for the MESSENGER LG2 sensor and both LP-NS sensors are compared in Fig. B1. The MESSENGER integrands are shown for three different times during the M1 flyby. Features seen in this plot are a thermal neutron enhancement due to the Doppler-filter effect (black trace for $E < 10^{-6}$ MeV), variations in the response due to spacecraft orientation and altitude (blue versus red and black traces for $E > 10^{-5}$ MeV), and the Cd cutoff at 0.4 eV in the LP Cd-covered sensor. For the purposes of validation, the most important part of this integrand is the power-law behavior for epithermal and fast neutrons. For the MESSENGER model, the integrand varies as $1/E^{1.043}$, while for LP it varies as $1/E^{1.395}$. The shallower MESSENGER response is likely due to the fact that the LG sensors are more closely located to neutron-moderating material (e.g., BC454 scintillator, spacecraft material) than the LP sensors. As a consequence, high-energy neutrons will interact with this material, lose energy, and be more efficiently detected than they would have been at their original energy. On a practical level, the power-law behavior demonstrates that while the LP–NS integral can be stopped at ~100 keV without a loss of accuracy from ignoring higher energies, the integration for MESSENGER should be calculated up to at least 10 MeV to ensure that the full response is properly taken into account.

As mentioned above, the validation with LP–NS data is an update to the validation given by Lawrence et al. (2006). Here, a new modeling code, as well as revised understanding of the GCR flux and ^{3}He sensor orientation are described. First, a reexamination of the south-pole neutron monitor count rate data used to determine the solar modulation parameter, ϕ, showed that $\phi = 360$ MV is a more appropriate value than the $\phi = 346$ MV used by Lawrence et al. (2006). An independent analysis of energetic particle flux data from the Advanced Composition Explorer showed that $\phi = 360$ MV holds for early 1998 (Wiedenbeck et al., 2009). Following McKinney et al. (2006), the GCR normalization constant for $\phi = 360$ MV is 5.54 protons cm^{-2} s^{-1}.

Another factor not fully explored by Lawrence et al. (2006) was sensor orientation. The raw LP–NS data had a latitude-dependent sensor response, and this latitude dependence was corrected to the effective response at the equator. However, in terms of modeling, the most convenient orientation is to set the long axis of the ^{3}He sensor perpendicular to the spacecraft velocity vector while viewing a pole, which here we call the "nominal" orientation. From the equator-to-pole latitude-correction factor of Fig. 25 of Maurice et al. (2004), we apply a factor of 640/705 = 0.9 to the modeled count rates. Finally, after applying other factors ($N_{MCNPX} = 1/4$ and a spacecraft altitude of 30 km), the modeled count rates are calculated for a FAN-type soil and shown in Table B1. Columns 2 and 3 show the measured and modeled count rates for the Cd- and Sn-covered sensors (the Cd sensor measured epithermal neutrons and the Sn-covered sensor measured thermal plus epithermal neutrons). The fractional differences between the measured and modeled Cd and Sn count rates are 13% and 18%, respectively.

Because LP was a rotating spacecraft with the spin axis perpendicular to the ecliptic, rotational information is available from the LP–NS data. The fifth and seventh columns of Table B1 show the modeled count rates for two different orientations measured through the LP spacecraft rotation. Fig. 30 of Maurice et al. (2004) shows the measured count rate as a function of rotation angle for both sensors. Column 5 gives the modeled count rate for a polar location where the sensor long axis is parallel to the spacecraft velocity, **V**. The fractional differences between this orientation and the nominal orientation (column 6) are similar to the variations seen in the measured data. Specifically, the Sn-covered sensor has a ~5% measured variation Maurice et al. (2004) due to the Doppler-filter effect, while the modeled variation is 6%. The Cd-covered sensor shows little to no variation in either the measured data or model. Column 7 shows the modeled count rate when the long axis is perpendicular to the velocity vector, **V**, and parallel to the spacecraft-to-Moon center vector, **r**. Here, a variation is seen in both the Cd and Sn sensors and is caused by a reduced sensor area

Table B1
Comparison of measured and modeled count rates for Cd and Sn, where the modeled count rates are listed for various orientations as described in the text.

	Measured (cps)	Long axis ⊥ to **V** Long axis ⊥ to **r** (nom. orientation)		Long axis || to **V** Long axis ⊥ to **r**		Long axis ⊥ to **V** Long axis || to **r**	
		Modeled (cps)	% Diff from meas.	Modeled (cps)	% Diff from nom.	Modeled (cps)	% Diff from nom.
Cd	20.5	23.2	13	23.1	−0.4	21.0	−9
Sn	47.0	55.6	18	52.5	−6	49.5	−11

that views the lunar surface. The modeled variations of 9% and 11% are similar to the measured values of 9–12% and 10–13%, respectively (Maurice et al., 2004).

In summary, the absolute modeled count rates match the measured data to better than 20%. The largest source of uncertainty in the modeled count rate is likely the chosen modulation parameter, which can be uncertain by up to ±100 MV (Usoskin et al., 2005; Wiedenbeck et al., 2009) depending on how it is determined. This uncertainty can easily account for differences of up to 25%. The relative variations with sensor orientation match the observation to within data error. Thus, within the uncertainties described above, the comparison of measured and modeled LP data validates the model calculation.

References

Bartol Research Institute, 2009. University of Delaware Bartol Research Institute Neutron Monitor Program. <http://neutronm.bartol.udel.edu/>.

Benz, W., Slattery, W.L., Cameron, A.G.W., 1988. Collisional stripping of Mercury's mantle. Icarus 74, 516–528.

Bevington, P.R., Robinson, D.K., 1992. Data Reduction and Error Analysis for the Physical Sciences, second ed. McGraw-Hill, New York. 328 pp.

Boynton, W.V., Sprague, A.L., Solomon, S.C., Starr, R.D., Evans, L.G., Feldman, W.C., Trombka, J.I., Rhodes, E.A., 2007. MESSENGER and the chemistry of Mercury's surface. Space Sci. Rev. 131, 85–104.

Cameron, A.G., 1985. The partial volatilization of Mercury. Icarus 64, 285–294.

Cloutis, E.A., Hardersen, P.S., Bish, D.L., Bailey, D.T., Gaffey, M.J., Craig, M.A., 2010. Reflectance spectra of iron meteorites: Implications for spectral identification of their parent bodies. Meteorit. Planet. Sci., in press.

Denevi, B.W., Robinson, M.S., 2008. Mercury's albedo from Mariner 10: Implications for the presence of ferrous iron. Icarus 197, 239–246.

Denevi, B.W., and 10 colleagues, 2009. The evolution of Mercury's crust: A global perspective from MESSENGER. Science 324, 613–619.

Elphic, R.C., Maurice, S., Lawrence, D.J., Feldman, W.C., Barraclough, B.L., Binder, A.B., Lucey, P.G., 1998. Lunar Fe and Ti abundances: Comparison of Lunar Prospector and Clementine data. Science 281, 1493–1496.

Elphic, R.C., Lawrence, D.J., Feldman, W.C., Barraclough, B.L., Maurice, S., Binder, A.B., Lucey, P.G., 2000. Determination of lunar global rare Earth abundances using Lunar Prospector Neutron Spectrometer observations. J. Geophys. Res. 105, 20333–20346.

Elphic, R.C., Lawrence, D.J., Feldman, W.C., Barraclough, B.L., Maurice, S., Lucey, P.G., Blewett, D.T., Binder, A.B., 2002. Lunar Prospector Neutron Spectrometer constraints on TiO_2. J. Geophys. Res. 107 (E4), 5024. doi:10.1029/2000JE001460.

Fegley Jr., B., Cameron, A.G.W., 1987. A vaporization model for iron/silicate fractionation in the Mercury protoplanet. Earth Planet. Sci. Lett. 82, 207–222.

Feldman, W.C., Drake, D.M., 1986. A Doppler filter technique to measure the hydrogen content of planetary surfaces. Nucl. Instrum. Methods, Section A 245, 182–190.

Feldman, W.C., Drake, D.M., O'Dell, R.D., Brinkley Jr., F.W., Anderson, R.C., 1989. Gravitational effects on planetary neutron flux spectra. J. Geophys. Res. 94, 513–525.

Feldman, W.C., Barraclough, B.L., Maurice, S., Elphic, R.C., Lawrence, D.J., Thomsen, D.R., Binder, A.B., 1998. Major compositional units of the Moon: Lunar Prospector thermal and fast neutrons. Science 281, 1489–1493.

Feldman, W.C., Lawrence, D.J., Elphic, R.C., Vaniman, D.T., Thomsen, D.R., Barraclough, B.L., Maurice, S., Binder, A.B., 2000. The chemical information content of lunar thermal and epithermal neutrons. J. Geophys. Res. 105, 20347–20363.

Gasnault, O., Feldman, W.C., Maurice, S., Genetay, I., d'Uston, C., Prettyman, T.H., Moore, K.R., 2001. Composition from fast neutrons: Application to the Moon. Geophys. Res. Lett. 28, 3797–3800.

Goettel, K.A., 1988. Present bounds on the bulk composition of Mercury: Implications for planetary formation processes. In: Vilas, F., Chapman, C.R., Matthews, M.S. (Eds.), Mercury. University of Arizona Press, Tucson, pp. 613–621.

Goldsten, J.O., and 23 colleagues, 2007. The MESSENGER Gamma-Ray and Neutron Spectrometer. Space Sci. Rev. 131, 339–391.

Lawrence, D.J., Elphic, R.C., Feldman, W.C., Prettyman, T.H., Gasnault, O., Maurice, S., 2003. Small area thorium features on the lunar surface. J. Geophys. Res. 108 (E9), 5102. doi:10.1029/2003JE002050.

Lawrence, D.J., Feldman, W.C., Elphic, R.C., Hagerty, J.J., Maurice, S., McKinney, G.W., Prettyman, T.H., 2006. Improved modeling of Lunar Prospector Neutron Spectrometer data: Implications for hydrogen deposits at the lunar poles. J. Geophys. Res. 111. E08001. doi:10.1029/2005JE002637.

Leary, J.C., and 17 colleagues, 2007. The MESSENGER spacecraft. Space Sci. Rev. 131, 187–217.

Lingenfelter, R.E., Canfield, E.H., Hampel, V.E., 1972. The lunar neutron flux revisited. Earth Planet. Sci. Lett. 16, 355–369.

Lodders, K., Fegley Jr., B., 1998. The Planetary Scientist's Companion. Oxford University Press. 321 pp.

Masarik, J., Reedy, R.C., 1996. Gamma ray production and transport in Mars. J. Geophys. Res. 101, 18891–18912.

Maurice, S., Feldman, W.C., Lawrence, D.J., Gasnault, O., d'Uston, C., Lucey, P.G., 2000. High-energy neutrons from the Moon. J. Geophys. Res. 105, 20365–20375.

Maurice, S., Lawrence, D.J., Feldman, W.C., Elphic, R.C., Gasnault, O., 2004. Reduction of neutron data from Lunar Prospector. J. Geophys. Res. 109. E07S04. doi:10.1029/2003JE002208.

McClintock, W.E., and 12 colleagues, 2008. Spectroscopic observations of Mercury's surface reflectance during MESSENGER's first Mercury flyby. Science 321, 62–65.

McCoy, T.J., Dickinson, T.L., Lofgren, G.E., 1999. Partial melting of the Indarch (EH4) meteorite: A textural, chemical, and phase relations view of melting and melt migration. Meteorit. Planet. Sci. 34, 735–746.

McKinney, G.W., Lawrence, D.J., Prettyman, T.H., Elphic, R.C., Feldman, W.C., Hagerty, J., 2006. MCNPX benchmark for cosmic-ray interactions with the Moon. J. Geophys. Res. 111. E06004. doi:10.1029/2005JE002551.

Morgan, J.W., Anders, E., 1980. Chemical composition of Earth, Venus, and Mercury. Proc. Natl. Acad. Sci. 77, 6973–6977.

National Nuclear Data Center, 2009. Evaluated Nuclear Data File (ENDF) <http://www.nndc.bnl.gov/exfor/endf00.jsp>.

Noble, S.K., Pieters, C.M., 2003. Space weathering on Mercury: Implications for remote sensing. Solar Syst. Res. 37, 31–35.

Pelowitz, D.B. (Ed.), 2005. MCNPX User's Manual, Version 2.5.0. Report LA-UR-94-1817, Los Alamos National Laboratory, Los Alamos, New Mexico, 473 pp.

Prettyman, T.H., Haggerty, J.J., Elphic, R.C., Feldman, W.C., Lawrence, D.J., McKinney, G.W., Vaniman, D.T., 2006. Elemental composition of the lunar surface: Analysis of gamma ray spectroscopy data from Lunar Prospector. J. Geophys. Res. 111. E12007. doi:10.1029/2005JE002656.

Solomon, S.C., and 10 colleagues, 2008. Return to Mercury: A global perspective on MESSENGER's first Mercury flyby. Science 321, 59–62.

Sprague, A., Warell, J., Cremonese, G., Langevin, Y., Helbert, J., Wurz, P., Veselovsky, I., Orsini, S., Milillo, A., 2007. Mercury's surface composition and character as measured by ground-based observations. Space Sci. Rev. 132, 399–431.

Sprague, A.L., Donaldson Hanna, K.L., Kozlowski, R.W.H., Helbert, J., Maturilli, A., Warell, J.B., Hora, J.L., 2009. Spectral emissivity measurements of Mercury's surface indicate Mg- and Ca-rich mineralogy, K-spar, Na-rich plagioclase, rutile, with possible perovskite and garnet. Planet. Space Sci. 57, 364–383.

Taylor, G.J., Scott, E.R.D., 2003. Mercury. In: Davis, A.M. (Ed.), Treatise on Geochemistry, Meteorites, Comets, and Planets, vol. 1. Elsevier, Amsterdam, The Netherlands, pp. 477–485.

Usoskin, I.G., Alanko-Huotari, K., Kovaltsov, G.A., Mursula, K., 2005. Heliospheric modulation of cosmic rays: Monthly reconstruction for 1951–2004. J. Geophys. Res. 110. A12108. doi:10.1029/2005JA011250.

Usselman, T.M., Lofgren, G.E., 1976. The phase relations, textures, and mineral chemistries of high-titanium mare basalts as a function of oxygen fugacity and cooling rate. Proc. Lunar Sci. Conf. 7, 1345–1363.

Wadhwa, M., 2008. Redox conditions on small bodies, the Moon and Mars. Rev. Mineral. Geochem. 68, 493–510.

Warell, J., Blewett, D.T., 2004. Properties of the Hermean regolith: V. New optical reflectance spectra, comparison with lunar anorthosites, and mineralogical modeling. Icarus 168, 257–276.

Weidenschilling, S.J., 1978. Iron/silicate fractionation and the origin of Mercury. Icarus 35, 99–111.

Wetherill, G.W., 1988. Accumulation of Mercury from planetesimals. In: Vilas, F., Chapman, C.R., Matthews, M.S. (Eds.), Mercury. University of Arizona Press, Tucson, pp. 670–691.

Wiedenbeck, M.E., and 13 colleagues, 2009, Time dependence of solar modulation throughout solar cycle 23 as inferred from ACE measurements of cosmic-ray energy spectra. In: Proceedings of the 31st International Cosmic Ray Conference, Lodz, Poland, http://icrc2009.uni.lodz.pl/proc/pdf/icrc0545.pdf.